

THE MEGAMASER COSMOLOGY PROJECT.VIII. A GEOMETRIC DISTANCE TO NGC 5765b

F. Gao^{1,2,3}, J. A. Braatz², M. J. Reid⁴, K. Y. Lo², J. J. Condon², C. Henkel^{5,6}, C. Y. Kuo⁷,
C. M. V. Impellizzeri^{2,8}, D. W. Pesce⁹ AND W. Zhao¹

ABSTRACT

As part of the Megamaser Cosmology Project (MCP), here we present a new geometric distance measurement to the megamaser galaxy NGC 5765b. Through a series of VLBI observations, we have confirmed the water masers trace a thin, sub-parsec Keplerian disk around the nucleus, implying an enclosed mass of $4.55 \pm 0.40 \times 10^7 M_{\odot}$. Meanwhile, from single dish monitoring of the maser spectra over two years, we measured the secular drifts of maser features near the systemic velocity of the galaxy with rates between 0.5 and 1.2 km s⁻¹ yr⁻¹. Fitting a warped, thin disk model to these measurements, we determine a Hubble Constant H_0 of 66.0 ± 6.0 km s⁻¹ Mpc⁻¹ with the angular-diameter distance to NGC 5765b of 126.3 ± 11.6 Mpc.

Apart from the distance measurement, we also investigate some physical properties related to the maser disk in NGC 5765b. The high-velocity features are spatially distributed into several clumps, which may indicate the existence of a spiral density wave associated with the accretion disk. For the red-shifted features, the envelope defined by the peak maser intensities increases with radius. The profile of the systemic masers in NGC 5765b is smooth and shows almost no structural changes over the two years of monitoring time, which differs from the more variable case of NGC 4258.

¹Key Laboratory for Research in Galaxies and Cosmology, Shanghai Astronomical Observatory, Chinese Academy of Science, Shanghai 200030, China

²National Radio Astronomy Observatory, 520 Edgemont Road, Charlottesville, VA 22903, USA

³Graduate School of the Chinese Academy of Sciences, Beijing 100039, China

⁴Harvard-Smithsonian Center for Astrophysics, 60 Garden Street, Cambridge, MA 02138, USA

⁵Max-Planck-Institut für Radioastronomie, Auf dem Hügel 69, 53121 Bonn, Germany

⁶King Abdulaziz University, P.O. Box 80203, Jeddah, Saudi Arabia

⁷Academia Sinica Institute of Astronomy and Astrophysics, P.O. Box 23-141, Taipei 10617, Taiwan

⁸Joint Alma Office, Alonso de Cordova 3107, Vitacura, Santiago, Chile

⁹Department of Astronomy, University of Virginia, P.O. Box 400325, Charlottesville, VA 22904, USA

1. INTRODUCTION

Recent measurements of the cosmic microwave background (CMB) anisotropies have provided dramatic confirmation of the “standard” Λ CDM model (e.g. Hinshaw et al. 2013). However, degeneracies between parameters such as the dark energy equation of state, the Hubble constant and the neutrino mass limit the determination of each quantity from the CMB data alone. One way to break this degeneracy is an independent and high precision measurement of H_0 (better than a few percent), as pointed out in Hu (2005). This motivation has reinvigorated efforts to measure H_0 and has driven the development of better methods of measuring H_0 over the past few years. For a general review on this topic, please see Freedman & Madore (2010) and references therein.

So far, measurements of H_0 have achieved about 3 % precision. Riess et al. (2011) derived $H_0 = 73.8 \pm 2.4 \text{ km s}^{-1} \text{ Mpc}^{-1}$ by using both Type Ia supernovae and Cepheids. Meanwhile, by improving the calibration of the period-luminosity (P-L) relation of Cepheids using mid-infrared observations, Freedman et al. (2012) obtained $H_0 = 74.3 \pm 2.1 \text{ km s}^{-1} \text{ Mpc}^{-1}$ from the Carnegie Hubble Program.

On the other hand, with the flat geometry assumption, the model-dependent prediction of H_0 from the most recent Planck result has a lower H_0 of $67.8 \pm 0.9 \text{ km s}^{-1} \text{ Mpc}^{-1}$ (Planck Collaboration XIII 2015), while the recent complete WMAP nine year observations constrain H_0 to be $70.0 \pm 2.2 \text{ km s}^{-1} \text{ Mpc}^{-1}$ (Hinshaw et al. 2013). Both of these predictions are in tension with the directly measured H_0 from Type Ia supernovae and Cepheids, as mentioned above. It is not clear so far whether this tension means new physics are needed, adding to the basic six parameter Λ CDM model, or any unknown systematic errors exist in either of the measurements. In either case, a direct measurement of H_0 independent of the methods mentioned above is highly desired.

As one of the direct distance measurement methods, the “disk maser” method has demonstrated its capability for precise distance measurement through the work on the archetypal disk megamaser galaxy NGC 4258 (e.g. Herrnstein et al. 1999; Humphreys et al. 2013). This method utilizes the 22 GHz water maser emission, which traces a sub-parsec thin accretion disk in Keplerian rotation at the center of a galactic nucleus, to obtain the angular-diameter distance. The maser distance to NGC 4258 provides an anchor point for the distance ladder using Cepheids and type Ia supernovae in Riess et al. (2011). When applied to more distant galaxies well into the Hubble flow, the disk maser method provides a simple, one-step measurement of H_0 that doesn’t involve secondary calibrations, which may introduce extra systematic errors.

With this motivation, the Megamaser Cosmology Project (MCP) aims to make an

independent measurement of H_0 to a few percent uncertainty by measuring the angular-diameter distances to disk megamaser galaxies well into the Hubble flow (between 50 and 200 Mpc). So far, the MCP group has published results on three galaxies, UGC 3789 with $H_0 = 68.9 \pm 7.1 \text{ km s}^{-1} \text{ Mpc}^{-1}$ (Reid et al. 2013), NGC 6264 with $H_0 = 68.0 \pm 9.0 \text{ km s}^{-1} \text{ Mpc}^{-1}$ (Kuo et al. 2013) and NGC 6323 with $H_0 = 73_{-22}^{+26} \text{ km s}^{-1} \text{ Mpc}^{-1}$ (Kuo et al. 2015). Measurement of distances for other megamaser-host galaxies and the search for more suitable distance measurement candidates are ongoing.

As part of the MCP effort, here we present a new geometric distance measurement to the megamaser galaxy NGC 5765b. NGC 5765b is an Sa-b galaxy in a galaxy pair together with NGC 5765a. It harbors a Seyfert 2 active galactic nucleus. The 22 GHz water maser emission was discovered in 2012 February during our survey observations using the Robert C. Byrd Green Bank Telescope (GBT)¹. Fig. 1 shows a representative GBT single-dish spectrum, which has a typical disk maser profile showing three sets of emission lines, indicating a rotation speed about 600 km s^{-1} . The recession velocity of NGC 5765b is $\sim 8345 \text{ km s}^{-1}$, which is well into the Hubble flow. In this paper, we use optical velocity defined in the LSR frame throughout. To convert to Heliocentric for NGC 5765b, subtract 12 km s^{-1} from the LSR velocity.

This paper focuses solely on the distance measurement to NGC 5765b and some physical properties of the maser disk specific to this galaxy. In a forthcoming paper, we will summarize the results from the four published galaxies measured by the MCP, present a combined H_0 measurement, and summarize plans to complete the project. We will compare H_0 from masers to that measured from other methods, and present updates on constraints of other cosmological parameters in the final summary paper.

This paper is arranged as follows: we report the VLBI observations and results in Section 2. Section 3 describes our single dish monitoring observations and the acceleration measurements. In Section 4 we describe the distance measurement with a Bayesian approach and give the fitting results and error budgets. In Section 5, first we discuss some essential requirements for good distance measurement based on the case of NGC 5765b. Then we focus on some physical properties seen in NGC 5765b, including the clumpiness of the red-shifted features, the correlation between maser flux and radius seen in the red-shifted features, and the variability of the systemic maser profile compared to the case of NGC 4258. We present our conclusions in Section 6.

¹The Green Bank Telescope is a facility of the National Radio Astronomy Observatory.

2. VLBI OBSERVATIONS

To map the spatial distribution of maser spots in NGC 5765b, we conducted a series of VLBI observations between 2012 April and 2014 January, with the 10 antennas of the Very Long Baseline Array (VLBA)², augmented by the 100m GBT, the Effelsberg 100m telescope (EB), and the Karl G. Jansky Very Large Array (VLA). We list all the basic observing information in Table 1, including project code, date observed, duration, antennas used, beam size, sensitivity, and the observing mode.

2.1. VLBI absolute position measurement for NGC 5765b

Following the detection of maser emission in NGC 5765b by the GBT, we conducted phase referencing VLBI observations (project code BB313AC and BB321Y5) to measure the maser’s sky position. Based on our experience, to maintain good phase coherence and calibration, we require an absolute position measurement for the NGC 5765b maser good to ~ 10 mas (see details in Appendix A). We followed the observation setup and data reduction process for phase-referencing observations as described in Reid et al. (2009). Two nearby quasars, J1448+0402 and J1458+0416, were chosen as phase reference calibrators and we cycled the observations between these 2 calibrators and NGC 5765b.

The data reduction was done with NRAO’s Astronomical Image Processing System (AIPS) software. From BB313AC we derived the sky position of the peak maser emission at velocity 8294.0 km s^{-1} , which is RA= $14^{\text{h}}50^{\text{m}}51^{\text{s}}.51950$ and DEC= $+05^{\circ}06'52''.2502$. We use this position in correlating later VLBI observations. The position difference we measured between BB313AC and BB321Y5 is 0.1 mas in RA and 0.7 mas in DEC, which is quoted as the measured absolute position uncertainty. We list the sky positions for all these 3 sources in Table 2.

2.2. New VLBI capability starting 2013 February

In general, our ability to measure the relative positions of megamaser spots with VLBI is limited by sensitivity, with the position uncertainty of each maser spot approximately given by $0.5\Theta/(S/N)$, in which Θ is the synthesized beam size, and S/N is the signal-to-noise ratio. To reduce the noise level would require a longer integration time and/or larger

²The VLBA is a facility of the National Radio Astronomy Observatory, which is operated by the Associated Universities, Inc. under a cooperative agreement with the National Science Foundation (NSF).

array collecting area. The typical intensity of maser emission in our targets is a few tens of mJy and line widths are $\sim 2 \text{ km s}^{-1}$. Based on our experience, mapping 10 mJy maser line requires a ~ 10 -hour VLBI observation using the VLBA+GBT+EB. The case of NGC 6323 further demonstrates the necessity of VLBI sensitivity, in which thirteen 12-hour VLBI tracks were conducted to map the <10 mJy systemic masers in NGC 6323 (Kuo et al. 2011), but in the end their sensitivity-limited VLBI measurement is still the limiting factor for determining H_0 as concluded in Kuo et al. (2015).

Our VLBI observations benefit from two significant upgrades which were implemented in 2013 February:

1) The VLBI observations were joined by the VLA in the phased-array mode, following the completion of the expanded VLA project. The phased-VLA is a key component in our VLBI observations as it improves our sensitivity by up to 40%.

2) As part of the VLBA sensitivity upgrade project, the new ROACH Digital Backend(RDBE), together with the Mark 5C recording system, replaced the old VLBA legacy system for all stations included in our observations. The new recorder increases the data recording rate from 512 Mbit s^{-1} to 2 Gbit s^{-1} , allowing us to use two 128 MHz bands to cover the whole maser spectrum contiguously, with dual polarization and 2-bit sampling. For comparison, with the recording rate of 512 Mbit s^{-1} and maximum bandwidth of each baseband limited to 16 MHz as before, we could barely cover the whole spectrum of NGC 5765b with the eight available basebands, as both the blue-shifted and red-shifted features span over 20 MHz in frequency. So the new system increases the sensitivity by increasing observation efficiency. For data correlation, in addition to the default “continuum-like” correlation pass with 0.5 MHz channel size over the whole band, we obtained a second correlation pass with three narrow bands of 32 MHz bandwidth centered on the three sets of maser lines using the new zoom-band mode offered in the DiFX software correlator. The spectral resolution in our raw data is 25 kHz ($\sim 0.3 \text{ km s}^{-1}$), which is comparable to that of our GBT single dish spectrum (24.4 kHz). This is 5 times finer than what we could achieve with the legacy system and it allows higher accuracy of matching between the single dish and VLBI spectra.

Except for the two VLBI tracks conducted in phase referencing mode when measuring the absolute position of NGC 5765b, all other VLBI observations were observed in the “self-cal” mode, in which we use the strongest maser line as the phase calibrator. Our observation setup and data reduction process are similar to previous MCP observations, so please refer to earlier papers (Reid et al. 2009; Kuo et al. 2013) for more details. Here we only describe differences from earlier work.

For the phased VLA, we need to “phase it up” prior to each VLBI scan. The “phase up” was done by observing J1448+040 (> 200 mJy, 1.1° away from NGC 5765b) for 1 minute between each VLBI scan. To maintain good phase coherence for the VLA, we set the maximum VLBI scan length to be 10 mins with the VLA in B or C configuration. We also added a flux calibration scan for the VLA to get the combined system temperature for the phased array. For all self-calibration tracks, we used the hourly observed delay calibrator to solve for the change of multi-band delay in time rather than using geodetic blocks as we do for phase-referenced tracks. After removing the instrumental delay, we ran FRING in AIPS on delay calibrators to solve for the multi-band delays and apply this correction to the target source.

In our 2013 and 2014 data, we noticed a fast fringe phase drifting over time and lower fringe amplitude on all GBT baselines on calibrator scans, after all calibrations were applied. To quantify this issue, we fit the fringe phase, delay and rate using the strongest maser lines in NGC 5765b (at velocity between 8294 and 8301 km s $^{-1}$, with flux > 100 mJy) on the GBT-VLA baseline with an integration time of 30s. Then we smoothed the fitted results with a boxcar window of 5 minutes and got a residual fringe rate (RFR) of ~ 4 mHz on the GBT over the whole observation. We repeated this measurement in all our VLBI datasets and found this RFR shows up on all calibrator scans and target scans, and it remains constant over the entire track and also between tracks. Finally we corrected the RFR using AIPS task CLCOR by adding in the rate correction before splitting the data for self-calibration.

After calibrating each of the tracks and doing preliminary imaging, we identified the best tracks and combined them in the following way: For data observed in early 2013, we combined data from BB321C, BB321E1, BB321F and BB321N in UV space, as they were observed within 2 months of each other. Likewise, for data observed in late 2013 until early 2014, we combined BB321T, BB321Y2, BB321Y3 and BB321Y4 in UV space. Then we combined these two maps in the image plane by applying a weighted average to their positions for each velocity channel, with each velocity channel matched within 0.3 km s $^{-1}$ between the two datasets. The channel size of the final datasets is ~ 1.7 km s $^{-1}$. The two maps were aligned by referencing to the position of the strongest feature in the systemic part of the spectrum, assuming they are the same feature with no position change (if we assume a Keplerian rotation velocity of 600 km s $^{-1}$ for the strongest feature, the sky position change of this feature over 1 yr is only ~ 0.001 mas). This gives the final VLBI map we use in the following analysis, as shown in Fig. 2.

2.3. VLBI observation results

In general, our VLBI map (Fig. 2) shows a linear configuration of all maser features along the position angle (P. A.) of 145° (defined with respect to the red-shifted masers, as measured from due north to the east). The position for each maser spot is referenced to the strongest line in the systemic part of the spectrum. By assuming a Hubble constant of $70 \text{ km s}^{-1} \text{ Mpc}^{-1}$ and recession velocity of 8345 km s^{-1} for NGC 5765b, we get a nominal distance of 119 Mpc. The high-velocity masers extend between 0.5 to 2.0 mas from the coordinate origin, which corresponds to ~ 0.3 to 1.2 pc. We note the blue-shifted and red-shifted features are distributed asymmetrically with respect to the systemic features, and the disk shows a clear warp in P.A. Maser spots on the red-shifted side are concentrated into 5 clumps, while the blue-shifted spots are more evenly distributed and are roughly divided into 2 parts. We discuss such clumpiness in more detail in Section 5.

The spatial distribution of maser spots in NGC 5765b is consistent with a thin-disk model. To check the kinematics of the maser disk, we construct the position-velocity (P-V) diagram by defining the impact parameter as $r = \sqrt{(x - x_0)^2 + (y - y_0)^2}$, in which x_0 and y_0 are the VLBI position for the strongest maser spot at $8295.91 \text{ km s}^{-1}$. Then we fit the high-velocity data with a Keplerian rotation curve, assuming an edge-on disk ($i_0=90^\circ$) with no inclination warping and also assuming that all the high-velocity maser spots are located along the midline (defined as the radial line through the disk perpendicular to the line of sight). The best fit yields an enclosed mass of $4.4 \pm 0.44 \times 10^7 M_\odot$, with the fitted recession velocity 8304 km s^{-1} and a position offset of the dynamic center of 0.011 mas in R.A. and -0.162 mas in DEC from the coordinate origin. In Fig. 3 we show the P-V diagram, which is centered on the fitted dynamic center. The best-fit Keplerian curve is overplotted as the dotted lines. Most of the high-velocity features deviate from the best-fit Keplerian curve by less than 5% of their rotation velocity. We treat this as the main contributor to the uncertainty on the black hole mass measurement since this simple model doesn't include fitting the inclination warp of the disk. So the final uncertainty for the black hole mass is about 10%.

While this simple model does not account for any inclination warping on the maser disk, the VLBI map and P-V diagram together still confirm that masers in NGC 5765b trace a thin, sub-parsec Keplerian disk. We treat these results as an initial guess for the central black hole mass, recession velocity and position of the dynamic center in the more detailed modeling of the maser disk (Section 4).

3. ACCELERATION MEASUREMENTS

3.1. Monitoring observations

To measure the secular drift of maser velocities in NGC 5765b over time, we obtained monthly GBT monitoring observations. Each observation lasted ~ 3 hours, from which we reach an rms noise of ~ 1.2 mJy, at a channel size of 24.4 kHz with Hanning smoothing. All together we obtained 18 epochs of observations from 2012 February to 2014 May, which bracket our VLBI observations. We list the details on the monitoring observations in Table 3. We note that because of a scheduling issue, we didn't get monitoring observations in 2014 January. Since our 2014 VLBI observation took place at this time, we used the VLBI spectrum to fill in that epoch. In this regard we have 19 epochs of data used in the acceleration measurements.

3.2. Acceleration of the systemic masers

3.2.1. Measuring “by eye”

We show all 19 epochs of monitoring spectra in Fig. 4, from which we can see the overall trend for line profile drifting and trace each individual component. As a first approximation, we use the peak of each distinct maser feature to trace the underlying acceleration. Those peaks were identified by eye and the results plotted in Fig. 5. From this, we get an initial estimate of the number of Gaussian components associated with the spectrum and the magnitude of the accelerations. From Fig. 5 it is clear that the systemic features can be traced easily over the two year monitoring period, and show distinct accelerations. The features between 8260 km s^{-1} and 8290 km s^{-1} all have similar accelerations of $\sim 0.6 \text{ km s}^{-1} \text{ yr}^{-1}$. Features outside that velocity range show more varied accelerations, between 0.5 and $1.2 \text{ km s}^{-1} \text{ yr}^{-1}$.

The “by eye” method does not adequately distinguish blended features. We also note that some systemic features (e.g. $\sim 8300 \text{ km s}^{-1}$ in the middle epochs) show a “negative” slope, which we think is not a sign of “negative” acceleration, but may have resulted from several lines blending together and the emerging of new peaks at different velocities, as the overall spectral profile shows a clear change (which is better illustrated in Fig. 4).

So we get initial estimates of line accelerations using the “by eye” method. We then use these estimates (only the positive ones) as the initial values in a least squares determination of accelerations, as described in the next section.

3.2.2. Method 1

To determine the best fit accelerations for each maser component, we decompose the overall profile into a series of Gaussian components and measure the drift of each component as the acceleration, using a least squares fitting algorithm. This is the so-called “Method 1” in previous MCP papers.

We follow the fitting process described in Reid et al. (2013), in which for the first step, we specify the velocity and acceleration for each component at a reference epoch, keep the line width fixed to 2 km s^{-1} (the typical line widths for the systemic masers in NGC 5765b are between 2 to 3 km s^{-1} , and here we use 2 km s^{-1} as an initial guess), and let the program set the amplitude of each component at the corresponding velocity from the real data. After this step, we have an initial mask of the Gaussian decomposition. We minimize the residual χ^2 between our Gaussian decomposition model and the real data by doing the fitting iteratively. In the second step, we fit the amplitude, width and velocity together for each component, but keep the acceleration unchanged. Finally we include the acceleration in the fitting and stop when the residual χ^2 reaches a stable minimum.

A visual inspection shows the systemic maser spectrum divides mainly into two parts around 8290 km s^{-1} , with the features between 8260 km s^{-1} to 8290 km s^{-1} (named “clump 1”) more distinct, while features between 8290 km s^{-1} to 8340 km s^{-1} (named “clump 2”) more blended, especially around 8295 km s^{-1} . So we fit the accelerations in the two clumps separately, with the procedure mentioned above. The final reduced χ^2 for the two clumps are 1.673 and 1.758, respectively. We note that since we have used Hanning smoothing for our data, the optimal reduced chi-squared value will not be unity.

We list the acceleration results from method 1 in Table 4 below.

3.2.3. Method 2

To check whether the results from Method 1 depend on the initial velocity and acceleration values, here we fit the accelerations using the more automated Method 2 (see more description in Reid et al. (2013)) in which the algorithm explores a wider range of initial parameters. Instead of specifying the number of components and the initial guess of velocity/width/acceleration for each component, here we only specify the velocity range for the fitting, the average width for each component and the average separation in velocity between each component. The program will generate multiple trials and do the fitting separately, with each trial using a set of initial values generated randomly for each of the components. We run the program with 100 trials to explore different starting points and keep the few

best solutions with small χ^2 and consistency with the results measured by eye. We show the fitting results in Fig. 6.

3.3. Error floor for accelerations of systemic masers

From previous MCP experience, to account for more realistic uncertainties in cases where the formal fitting uncertainty from method 1 is unrealistically small (e.g. less than $0.05 \text{ km s}^{-1} \text{ yr}^{-1}$ in the case of NGC 5765b), we use an “error floor” on the acceleration result and add that in quadrature to the formal fitting error to get the final uncertainty for each measured acceleration. However, a single value for the “error floor” might not be suitable for all maser features in the case of NGC 5765b. It is clearly shown in both Fig. 4 and Table 4 that the spectral features in clump 1 are more distinct and accurately measured, while those in clump 2 are more blended and show bigger scatter. Since line blending is an important contributor to the uncertainties, a large error floor here which may accurately represent the errors in clump 2 would down-weight results from clump 1, while a small error floor will overweight results from clump 2 in the other way. So for this galaxy we use the difference between results from method 1 and method 2 for each measured maser spot as an estimate of the error floor for each component.

We plot the acceleration fitting results from both methods in Fig. 6 for comparison.

3.4. Accelerations of the high-velocity masers

The high velocity features are not as highly blended as the systemic ones. Considering their relative weakness and their short lifetime (some of the blue-shifted features are only evident for 2 to 3 epochs), we measured their accelerations using only the “by eye” method. We list these results in Table 5.

Besides the formal fitting error, we also calculate the rms scatter in both the red-shifted and blue-shifted results, which are $0.155 \text{ km s}^{-1} \text{ yr}^{-1}$ (red) and $0.275 \text{ km s}^{-1} \text{ yr}^{-1}$ (blue) and $0.200 \text{ km s}^{-1} \text{ yr}^{-1}$ (combined). Overall, most of the measured results are within this rms level, with only maser features at $8856.32 \text{ km s}^{-1}$ and $7582.95 \text{ km s}^{-1}$ showing clear offsets from zero acceleration. For a high-velocity feature with rotation velocity of 600 km s^{-1} in NGC 5765b, an acceleration of $0.2 \text{ km s}^{-1} \text{ yr}^{-1}$ along the LOS direction requires a 16° deviation from the midline on the disk. Thus we conclude that most of the high velocity features locate on the mid-line (the diameter through the disk perpendicular to the line of sight) of the maser disk with deviations less than $\sim 16^\circ$, with few exceptions.

4. DETERMINATION OF H_0

4.1. Model fitting of the accretion disk

To reconstruct the geometry and spatial distribution of maser spots from the observed data, here we fit a warped disk model to the VLBI and acceleration data, using a Bayesian approach. This model can accommodate 14 global parameters describing the disk geometry, including the Hubble constant H_0 , the central black hole mass M , position of the dynamic center on the sky X_0 & Y_0 , recession velocity and peculiar velocity of the galaxy V_0 & V_p , position angle and first/second order of warping on the P.A. direction PA , $\partial p/\partial r$, $\partial^2 p/\partial r^2$, inclination angle and first/second order of warping on the inclination direction i , $\partial i/\partial r$, $\partial^2 i/\partial r^2$ and two additional parameters describing the eccentricity of the disk e and the change of the azimuth angle for the major axis of the elliptical with radius $\partial p_{az}/\partial r$. Apart from these global parameters, there are also two parameters (r and ϕ) describing the coordinates on the disk for each maser spot. The input data for the model consists of the sky position, velocity and acceleration for each maser spot. The program uses a Markov chain Monte-Carlo (McMC) approach to sample the parameter space and applies the Metropolis-Hastings algorithm to explore the probability distribution function for each of the global parameters. To better sample parameter space, the program allows multiple “strands”, defined as independent runs of the McMC with different starting conditions, to run simultaneously. A more detailed description about the disk model and fitting process can be found in Reid et al. (2013) and Humphreys et al. (2013).

All together there are 212 maser spots mapped for NGC 5765b. We list the input data in Table 6. We estimated the initial value for the position angle, black hole mass, recession velocity and black hole position from our fitting of the P-V diagram in Section 2, while the initial value for H_0 in each strand was evenly selected between 60 and 80 $\text{km s}^{-1} \text{Mpc}^{-1}$. Except for recession velocity and peculiar velocity, we didn’t include a prior uncertainty in any other global parameters as we try to keep our fitting result away from any existing bias. We also note that even though the initial value for H_0 was chosen between 60 and 80 $\text{km s}^{-1} \text{Mpc}^{-1}$, H_0 could vary to any number as there are no constraints on it during each trial of fitting.

NGC 5765b sits in a galaxy pair together with NGC 5765a, and the recession velocity for each of them are (a) 8469 km s^{-1} and (b) 8345 km s^{-1} . Assuming the dynamic center of this galaxy pair has the averaged recession velocity of 8401 km s^{-1} , then the additional uncertainty in peculiar velocity caused by this galaxy pair is $\sim 70 \text{ km s}^{-1}$, which is less than 1% of the recession velocity of NGC 5765b. Apart from this, we don’t have any constraints on whether NGC 5765b deviates from the Hubble flow. Nevertheless, we include the peculiar

velocity in our fitting so that the uncertainty of peculiar velocity contributes appropriately to our final uncertainty in H_0 . As a conservative treatment, we use a peculiar velocity of zero with prior uncertainty of 250 km s^{-1} in our final fitting.

In our final model fitting we use 10 global parameters, where we have excluded the second order of warping in both the P.A. and inclination directions, and the two parameters for eccentricity, as they were insignificant to the final result. We use 10 strands in our fitting, with each strand containing 2×10^8 trials, which is sufficient to reach convergence. The convergence is indicated by the autocorrelation (AC) function for each model parameter. We require the AC function to drop near zero before 40% of the largest lag number. The largest lag number is defined as 25% of the maximum number of MCMC trials that have been recorded for each strand. Usually if 6 or 7 out of the total 10 strands have converged, we consider the total fitting result as converged. We show an example plot of the H_0 versus trial iteration number for several strands in Fig. 7. Another example of the AC function with lag number and also the H_0 probability distribution for the same strands are shown in Fig. 8.

To come to our final result, we dropped the first 20% of trials in each strand to avoid using any un-converged trials in the final probability distribution. For each of the global parameters, we quote the mean value in the probability distribution function as the fitted result, and 68% confidence range as the error. All uncertainties listed here have been scaled by $\sqrt{\chi^2/N}$, i.e., $\sqrt{1.575}$. For H_0 , we determine $66.0 \pm 5.0 \text{ km s}^{-1} \text{ Mpc}^{-1}$. We list the full set of final fitting results in Table 7. We also plot the probability distribution for each global parameter in Fig. 9, and show the distribution of maser features on the disk in Fig. 10.

4.2. Systematic uncertainty in H_0

Apart from the formal fitting uncertainty for H_0 , here we investigate several factors that might cause systematic uncertainty.

To test for human bias in the acceleration measurement, here we fit the maser disk using accelerations determined using method 2, rather than method 1, while still using the difference between the two methods as the error floor for acceleration data. This fit gives $H_0 = 68.5 \pm 6.0 \text{ km s}^{-1} \text{ Mpc}^{-1}$, which is consistent within $1\text{-}\sigma$ of our original result.

For the systemic features, the error floor we used for the acceleration data is the measured difference between results using method 1 and method 2, for each maser spot independently. To test the robustness of our measurement against the value of the error floor, we also tried setting the error floor to the mean difference between method 1 and method

2, calculated separately for clump 1 and clump 2. The mean difference in clump 1 is $0.045 \text{ km s}^{-1} \text{ yr}^{-1}$, and for clump 2 the value is $0.20 \text{ km s}^{-1} \text{ yr}^{-1}$. We re-run the Bayesian fitting with other parameters unchanged and get $H_0 = 68.0 \pm 6.4 \text{ km s}^{-1} \text{ Mpc}^{-1}$, consistent with our original result.

The error floor we used for the acceleration of high-velocity features is the mean of the rms values measured for the red-shifted and blue-shifted features. The rms for the red-shifted features is $0.155 \text{ km s}^{-1} \text{ yr}^{-1}$, while the blue-shifted features had an rms of $0.275 \text{ km s}^{-1} \text{ yr}^{-1}$. If we use $0.155 \text{ km s}^{-1} \text{ yr}^{-1}$ as the error floor only for the red-shifted masers and $0.275 \text{ km s}^{-1} \text{ yr}^{-1}$ only for the blue-shifted masers, we get $H_0 = 66.5 \pm 5.7 \text{ km s}^{-1} \text{ Mpc}^{-1}$, which is consistent to within $1\text{-}\sigma$ of our original result of $66.0 \pm 5.0 \text{ km s}^{-1} \text{ Mpc}^{-1}$.

The clumpiness of the high-velocity masers on the VLBI map suggests the existence of spiral structure in the accretion disk of NGC 5765b (see the next section for a detailed discussion). This phenomenon has been discussed for the maser disk of NGC 4258 (Humphreys et al. 2013), in which the unmodeled spiral structure is claimed to contribute 1% uncertainty for the final distance determination. Here we simply estimate that spiral structure in NGC 57675b similarly contributes 1% to the final error budget.

After including these sources of systematic uncertainty, our final measurement gives H_0 of $66.0 \pm 6.0 \text{ km s}^{-1} \text{ Mpc}^{-1}$. We list all the detailed uncertainties in Table 8.

5. DISCUSSION

5.1. Essential requirements for good distance measurements

Combined with our previous experience, we note that a good distance measurement (with uncertainty less than 10 %) using the “disk maser” method requires both a well-defined rotation curve from the high-velocity maser components and well-measured accelerations over a wide velocity range for the systemic masers. In principle, only one systemic feature with a perfectly measured acceleration could provide the distance, since the rotation curve defined by the high-velocity features measures the enclosed mass, the dynamic center and recession velocity. In practice, a large spread of systemic features over a wide velocity range not only reduces the mean acceleration measurement uncertainty, but also traces the inclination warping with masers at different radii. The case of NGC 5765b fulfills such requirements in the following aspects:

1. The system has bright maser lines, benefitting VLBI calibration and imaging.

A minimum maser line flux of $\sim 100 \text{ mJy}$ is required to get a solid fringe detection for

the VLBA+GBT array, within 1-2 mins integration time and 125 kHz channel size under moderate atmospheric conditions. For the VLBA+GBT+VLA array, this limit goes down to ~ 50 mJy. In the case of NGC 5765b, the strongest maser line is about 200 mJy, which is ideal to provide sufficient calibration of the atmospheric and instrumental effects.

As mentioned in Section 2.2, the relative position uncertainty of each maser spot is approximately given by $0.5\Theta/(S/N)$. For NGC 5765b, the blue-shifted features are the faintest, with most of them being below 15 mJy (as shown in Fig. 1). The systemic masers for which the acceleration has been measured are almost all above 20 mJy. The 1σ noise level from our VLBI map is $0.3 \text{ mJy beam}^{-1} \text{ channel}^{-1}$ (with a channel width of 125 kHz), providing a 10σ measurement of features at 3 mJy. Compare this to the Kuo et al. (2015) result on NGC 6323, where the systemic masers (which are weaker than the high-velocity masers in that galaxy) are all below 10 mJy. The authors conclude their final uncertainty ($\sim 30\%$) on the distance measurement is dominated by the low precision of the maser position measurements, even though their VLBI map has a noise level similar to that in our study.

It is also advantageous that our VLBI observations were scheduled closely in time (within 2 months) in both 2013 and 2014, which limits the impact of maser variability when combining tracks.

2. The maser covers a wide velocity range in both the systemic and high-velocity masers.

As mentioned in Section 2.2, the rotation curve traced by the high-velocity features defines M/D , where M is the enclosed mass and D is the distance, while the slope of the systemic features on the P-V diagram constrains M/D^3 . So a wider velocity coverage on both the systemic and high-velocity features provides better leverage and hence better constraints on M and D . In the case of NGC 5765b, the red-shifted and blue-shifted masers span over 350 km s^{-1} and 250 km s^{-1} respectively, and sample the rotation curve very well, as shown in Fig. 3.

The systemic masers in NGC 5765b span 90 km s^{-1} , and we are able to measure the acceleration of each line with a typical uncertainty of $\sim 10\%$ within 70 km s^{-1} velocity range. For comparison, in NGC 4258 the systemic features span over 110 km s^{-1} (Humphreys et al. 2008), contributing to the 3% distance measurement (Humphreys et al. 2013).

3. Accelerations of the systemic features are measured accurately.

In NGC 5765b, the low variability among the systemic features and relatively low ($< 1.5 \text{ km s}^{-1} \text{ yr}^{-1}$) but similar drift rate for the majority of features allows us to trace them through all observing epochs and contributes to our precise acceleration measurements. However, the monitoring must span a longer time to measure these low accelerations. The lifetimes

of individual maser components in other galaxies varies from a few months to a few years. In NGC 5765b the systemic masers have shown little structural changes over the observed 2.5 years, which has allowed us to utilize all 2.5 years of monitoring data to analyze each component.

We also note that the low variability and small accelerations in NGC 5765b reduce the impact of the summertime gap with GBT monitoring data. For maser galaxies with high accelerations or variability, it would be better to fill the summer gap for the best acceleration measurements.

5.2. Improving the H_0 estimate with future NGC 5765b observations

In this section we investigate chances to improve the H_0 measurement with observations of NGC 5765b in the future. The constraint on H_0 from this work is 9.1 %, with random uncertainties dominating the final result rather than systematic uncertainties, as listed in Table 8. So in principle, the final result could be improved by more observations. Since we use the same methodology for our distance measurement as Humphreys et al. (2013) for NGC 4258, which reached a 2.2 % formal fitting uncertainty and a 3 % total uncertainty, we compare the input data for both NGC 4258 and NGC 5765b quantitatively in this section.

The input data for the Bayesian fitting program we used here are the sky position, velocity and acceleration with individual uncertainties for each maser spot. The input data can be improved in two ways, by observing more maser spots covering a wider velocity range or by smaller uncertainties for each type of data.

We list the details of input data for both NGC 4258 and NGC 5765b in Table 9 for comparison. Regarding the velocity coverage, the most noticeable difference is the velocity range for the systemic part with accelerations measured: 110 km s⁻¹ in NGC 4258 versus 70 km s⁻¹ in NGC 5765b. For the high-velocity features, the velocity coverage is similar, which means a similar sampling range of the Keplerian rotation curve as NGC 4258 and NGC 5765b have similar black hole masses. Due to the relatively high intensity of the systemic masers in NGC 5765b and the noise level we reached here (1σ of 0.3 mJy beam⁻¹ channel⁻¹ (125 kHz) for the VLBI map, and < 2 mJy channel⁻¹ (24.4 kHz) for the single dish monitoring spectra), increasing either VLBI or single dish observing sensitivity will not substantially cover new velocities. So as a practical matter, it would be difficult to improve the overall fitting result by including more maser spots.

On the other hand, regarding the uncertainty for each type of data, the most noticeable difference between NGC 5765b and NGC 4258 lies in the acceleration data. For NGC

4258, the uncertainty on acceleration for each measured maser component is less than 4% (Humphreys et al. 2008), while for NGC 5765b the typical uncertainty is 10% for each maser component. The VLBI position uncertainties are similar between NGC 4258 and NGC 5765b, after adding the position error floor. So we conclude that future improvement of the H_0 uncertainty with NGC 5765b depends on measuring accelerations with better precision.

5.3. Clumpiness of the high-velocity masers

A visual inspection of the GBT spectrum (insets in Fig. 1) of the high-velocity components reveals the maser lines are regularly clustered into several clumps. This is especially obvious on the red-shifted features, in which there are mainly five clumps evenly distributed between 8740 km s^{-1} and 8980 km s^{-1} , spaced by $\sim 50 \text{ km s}^{-1}$. Beyond this, there is another clump centered at 9075 km s^{-1} .

The VLBI map (Fig. 2) shows that the red-shifted masers are also spatially clustered into several clumps, with a typical spacing between clumps of $\sim 0.3 \text{ mas}$ (0.18 pc). The blue-shifted masers, meanwhile, are distributed more smoothly and mainly appear in 2 clumps.

Such clumpiness of the high-velocity masers has been seen in several disk maser systems (e.g. NGC 4258 by Humphreys et al. (2008) (2013); UGC 3789 and NGC 2960 by Kuo et al. (2011)) but only discussed in detail for NGC 4258. We note that the spacing of clumps appears to be similar between the red and blue side of the disk only in the case of NGC 4258. Another thing to note is that the features in NGC 4258 appear clumped in radial arcs as shown in Humphreys et al. (2013), while for NGC 5765b, they appear clumped in both radius and azimuthal angle, as shown in Fig. 10.

Several models have been proposed to explain the generation of such clumpiness, including a spiral density wave model (Maoz 1995) and a spiral shock model (Maoz & McKee 1998).

The spiral shock model proposed that masers are generated in spiral shock regions and this could explain the asymmetry of the intensity between the red-shifted and blue-shifted features, as first seen in NGC 4258. This model also predicts that the red-shifted features will have negative accelerations, while the blue-shifted features have positive accelerations. In the case of NGC 5765b, the weighted average accelerations of the high-velocity features are (red-shifted) $0.008 \pm 0.155 \text{ km s}^{-1} \text{ yr}^{-1}$ and (blue-shifted) $-0.049 \pm 0.275 \text{ km s}^{-1} \text{ yr}^{-1}$. These results are consistent with zero acceleration, though with large measurement uncertainties. One particular blue-shifted feature at $7582.95 \text{ km s}^{-1}$ has an acceleration of -0.528 ± 0.110

$\text{km s}^{-1} \text{ yr}^{-1}$, which is inconsistent with predictions from the spiral shock model. So even though the red-shifted features are brighter than the blue-shifted features in NGC 5765b, our acceleration results do not support the spiral shock model. In a parallel MCP paper, Pesce et al. (2015) systematically examine the predictions from this model using all the disk maser spectra obtained from the MCP, and they do not find clear evidence supporting this model.

The spiral density wave model proposed that spiral structures are generated from non-axisymmetric perturbations on the accretion disk and maser clumps are located at the intersection of the spiral arms and the disk mid-line. So the high-velocity masers would be distributed within a few degrees from the mid-line and would have very small LOS accelerations that can be slightly positive or negative. This model works well for NGC 4258, where the maser clumps for both the red-shifted and blue-shifted features are periodic in disk radius with the same characteristic scale of ~ 0.75 mas (e.g. Humphreys et al. 2008). In the case of NGC 5765b, even though the red-shifted features are clustered into several clumps with an spacing of ~ 0.3 mas, the blue-shifted features do not show the same spacing (as shown in Fig. 2). So more precise measurements are needed to test the spiral density wave model in NGC 5765b.

5.4. Amplitude vs. position for the high-velocity masers

Bragg et al. (2000) compared the maser flux with maser position in NGC 4258, where no dependence between line amplitude and radius was found. Instead, they found that the maser amplitude peaks around the midline. This was interpreted as masers originate in aligned clumps of material that amplify each other, so the observed amplitude is largely independent of radius.

To test these results for NGC 5765b, we plot the maser amplitude versus disk radius and versus deviation from the mid-line for the high-velocity masers in NGC 5765b in Fig. 11. The flux comes from the VLBI map, which represents the mean maser intensity over our VLBI observations. The radius comes from the Bayesian fitting result for each maser spot.

It is interesting that for the red-shifted lines, the peak intensities of maser lines are proportional to their radius, and masers peak away from the midline. We use a power-law function to fit the outline of the peak intensities versus radius for the red-shifted features and the best fit yields a power index of 0.70 ± 0.050 (1σ), as shown by the solid line on the plot.

To see whether our fitted results are specific to the VLBI data only, we also use the

GBT monitoring data for a consistency check: We measure the peak intensity closest (within 1 km s^{-1}) to the velocities where the VLBI intensity peaks, namely 8753.8 km s^{-1} , 8856.0 km s^{-1} , 8968.5 km s^{-1} , 9077.5 km s^{-1} , 9079.0 km s^{-1} and 9081.3 km s^{-1} , and use these data to re-fit the power index for each epoch of the monitoring observations. The mean power law index is 0.75 ± 0.014 (1σ). So the power index we measured from the VLBI data is consistent with this result to within 3σ .

Intuitively, this positive flux-radius dependency seems natural. The LOS velocity of the high-velocity masers goes as $V_{rot} \cdot \cos(\phi)$, where V_{rot} is the Keplerian rotation speed and ϕ is the angular deviation from the mid-line. To maintain a velocity coherence of $\sim 1 \text{ km s}^{-1}$ required for maser amplification, maser spots with higher rotation velocities (thus closer to the dynamic center) would have shorter gain length. This would result in masers at higher rotation velocity having lower intensity by assuming the maser intensities are proportional to the gain length. If we assume the maser is saturated, a detailed calculation (see Appendix B) shows the maser flux goes with radius as $f \propto r^{1.5}$ with the maser flux linearly proportional to the gain length. For comparison, we plot the fitted curve with the power index fixed to 0.5 (dotted line) and 1.5 (dashed line) in Fig. 11 (a).

Since the fitted power index is inconsistent with the calculation above, a better explanation is needed. The maser flux may not scale with the gain length linearly, as the maser might be partially saturated. Also we didn't include the disk warping in our calculation, which would re-shape the regions where maser flux peaks. The disk warping may also cause the line peaks to deviate from the mid-line. Another factor that should be taken into account is the different gas and dust temperatures at different radii, which would have a significant effect on the maser pumping efficiency (e.g. Yates, et al. (1997)).

Pesce et al. (2015) compiled a list of 32 clean³ megamaser disk systems discovered so far and present their time-averaged single dish spectra. Six of these maser systems show a similar dependency of maser flux on radius as we have seen in the red-shifted part of NGC 5765b here. They are: J0437+2456 (blue-shifted), UGC 3789 (blue-shifted), ESO269-G012 (blue-shifted), UGC 9639 (blue-shifted), NGC 6264 (red-shifted) and CGCG498-038 (red-shifted).

³Here “clean” disk means that maser emission generated from the Keplerian disk dominates over that generated from jets or outflows, and the disk itself displays Keplerian rotation.

5.5. Beaming angle of the systemic masers

The slope of the systemic features on the P-V diagram is related to the physical radius of those spots to the dynamic center ($\sqrt{GM/r^3}$). From the P-V diagram, we fit a slope of $435.7 \text{ km s}^{-1} \text{ mas}^{-1}$. Combined with the black hole mass of $4.4 \times 10^7 M_\odot$ and nominal distance of 119 Mpc, this result corresponds to 0.68 pc. The Keplerian rotation velocity at this radius is about 530 km s^{-1} .

The systemic masers span 90 km s^{-1} in NGC 5765b (from 8240 to 8330 km s^{-1}). For simplicity, if we assume all the systemic features are located at the same radius, this would give a beaming angle of 9.8° on the azimuth direction for the systemic masers. However, since not all the systemic masers lie on the same radius, as shown by our Bayesian fitting result, here instead we use the velocity range of 8260 to 8290 km s^{-1} , in which masers are located at a similar radius of about 1 mas on the disk, to estimate the lower limit of the beaming angle. This gives an azimuthal beaming angle of 3.3° .

For comparison, among the other published megamaser disk systems, only two have azimuthal beaming angles estimated. NGC 4258 has a beaming angle of 7° , measured both by the slope of the systemic features (Miyoshi et al. 1995) and by monitoring the drift of systemic features’s velocity with time (Moran 2008). For UGC 3789, based on the slope of the systemic features on the P-V diagram by Braatz et al.(2010), we estimate the beaming angle to be 4.4° and 2.5° respectively for the two maser rings, as described in Braatz et al. (2010).

5.6. The profile and variability of systemic masers in NGC 5765b compared to NGC 4258

The profile of the systemic masers in NGC 5765b is smooth compared to the “spiky” high-velocity masers. This contrast is more obvious than the case of NGC 4258. One might consider whether the blended/“spiky” difference arises because the systemic features are amplifying the background radio continuum emission. Also since the systemic features all have similar LOS velocity, their velocities overlap and the total spectral profile is likely the sum of weak maser emission coming from numerous gas clouds in the accretion disk. The high-velocity masers meanwhile are self-amplified, and the spikiness may reflect a sparse availability of seed photons and different gain paths.

Another feature of the systemic maser spectrum is that there is little change of the overall profile across the observed 2.5 yrs as shown in Fig. 4, unlike the case of NGC 4258, which has shown clear structural changes on a few-months time scale (e.g. Argon et al.

2007). The “notches” and “dents” formed between strong features in the systemic part in NGC 5765b (especially between 8260 and 8290 km s⁻¹) co-drift with the maser peaks. This means the masing gas clouds are distributed closely with each other spatially, and they lie on a similar radius, which will have similar accelerations. This is consistent with the Bayesian fitting results, in which masers in the velocity range of 8260 and 8290 km s⁻¹ are all located at radii between 0.895 to 1.126 mas on the disk.

The black hole masses for NGC 4258 ($4.0 \times 10^7 M_\odot$ from Humphreys et al. 2013) and NGC 5765b ($4.55 \times 10^7 M_\odot$ from this work) are similar. The systemic maser spots in NGC 4258 are distributed around 0.14 pc in radius on the disk, while for NGC 5765b, systemic masers cover a larger range of radii, from 0.39 to 0.64 pc. As mentioned by Wallin et al. (1999), the change of the velocity field on the LOS direction may be the main reason for the spectral variability, so maser spots at larger radii would have a smaller change in the LOS velocity field in a certain amount of time according to the Keplerian rotation, thus showing less spectral variation. Qualitatively, the variabilities seen in NGC 4258 and NGC 5765b are consistent with this explanation.

Other explanations for maser variability include the change of the local physical conditions for pumping the masers and variability of the background continuum source which is particularly important if the masers are unsaturated. The persistence of the systemic masers in NGC 5765b might therefore be a result of a less variable background source, or an indication that the maser is saturated.

If the change of the LOS velocity field is the main reason for maser variability, future observations might be able to detect a correlation between maser variability and acceleration for the systemic features in all disk maser systems, since the acceleration depends on the radius.

5.7. Searching for the background radio continuum emission

As mentioned above, systemic masers in NGC 5765b may amplify the background radio continuum emission. We searched for radio continuum emission from the line-free channels in our VLBI dataset, but did not detect continuum emission at an upper limit of 0.1 mJy at 22 GHz. However, our recent VLA observation of NGC 5765b reveals a continuum flux of 5 mJy at 22 GHz. Also, a point source is detected with an integrated flux of 13.45 mJy at 1.4 GHz from the FIRST survey. So either the 22 GHz radio continuum emission associated with NGC 5765b is compact and variable, falling below our detection limit during the VLBI observations, or the emission has been resolved by the VLBI observations.

6. CONCLUSIONS

We present here the geometric distance measurement to the megamaser disk host galaxy NGC 5765b, as part of the Megamaser Cosmology Project (MCP). Owing to the relatively strong maser emission (> 200 mJy), new VLBI capabilities, and slow but discrete accelerations of the systemic masers, we are able to measure the distance with very high precision, from which we determine $H_0 = 66.0 \pm 6.0$ km s $^{-1}$ Mpc $^{-1}$ and an enclosed mass of $4.55 \pm 0.40 \times 10^7 M_\odot$. The case of NGC 5765b demonstrates essential requirements for good distance measurements (< 10 % uncertainty), which can serve as guidelines for future distance measurement work.

We also investigate some of the physical properties of the maser disk in NGC 5765b: the red-shifted and blue-shifted features are spatially clustered into several clumps with different characteristic scales on the red and blue sides. Combined with the acceleration measurements, these results favor the spiral density wave model, while the spiral shock model is not supported. We find that the peak maser amplitude depends on radius in the red-shifted features. NGC 5765b shows little variation of the systemic maser profile over the two years of observation. This is quite different compared to the case of NGC 4258. If variability is dominated by the change of the LOS velocity field due to Keplerian rotation, we expect to see a positive correlation between systemic maser variability and acceleration. This hypothesis could be tested within current disk maser systems.

REFERENCES

- Argon, A. L., Greenhill, L. J., Reid, M. J., Moran, J. M. & Humphreys, E. M. L. 2007, *ApJ*, 659, 1040
- Freedman, W. L. & Madore, B. F. 2010, *ARA&A*, 48, 673
- Freedman, W. L., Madore, B. F., Scowcroft, V., et al. 2012, *ApJ*, 758, 24
- Bragg, A. E., Greenhill, L. J., Moran, J. M. & Henkel, C. 2000, *ApJ*, 535, 73
- Hinshaw, G., Larson, D., Komatsu, E., et al. 2013, *ApJS*, 208, 19
- Herrnstein, J. R., Moran J. M., Greenhill, L. J., et al. 1999, *Nature*, 400, 539
- Hu, W. 2005, in *ASP Conf. Ser. 339, Observing Dark Energy*, eds. S. C. Wolff & T. R. Lauer (San Francisco, CA: ASP), 215

- Humphreys, E. M. L., Reid, M. J., Greenhill, L. J., Moran, J. M. & Argon, A. L. 2008, ApJ, 672,800
- Humphreys, E. M. L., Reid, M. J., Moran, J. M., Greenhill, L. J. & Argon, A. L. 2013, ApJ, 775,13
- Kuo, C. Y., Braatz, J. A., Condon, J. J. et al. 2011, ApJ, 727, 20
- Kuo, C. Y., Braatz, J. A., Reid, M. J. et al. 2013, ApJ, 767, 155
- Kuo, C. Y., Braatz, J. A., Lo, K. Y. et al. 2015, ApJ, 800, 26
- Maoz, E., 1995, ApJ, 455, L131
- Moran, J. M., 2008, ASPC, 395, 87
- Pesce, D. W., Braatz, J. A., Condon, J. J. et al, submitted
- Reid, M. J., Braatz, J. A., Condon, J. J. et al. 2009, ApJ, 695, 287
- Reid, M. J., Braatz, J. A., Condon, J. J. et al. 2013, ApJ, 767, 154
- Riess, A. G., et al. 2011, ApJ, 730, 119
- Planck Collaboration, Ade, P. A. R., Aghanim, N., et al. 2015, arXiv:1502.01589
- Suyu, S. H., Auger, M. W., Hilbert, S., et al. 2013, ApJ, 766, 70
- Wallin, B. K., Watson, W. D. & Wyld, H. D., 1999, ApJ, 517, 682
- Yates, J. A., Field, D. & Gray, M. D., 1997, MNRAS, 285, 303

A. Requirement on absolute source position accuracy in MCP VLBI observations

For a given baseline B , the interferometric phase of a target source at direction S and observing frequency ν_o is given by $\phi_o = 2\pi\nu_o \frac{B \cdot S}{c}$. During data cross-correlation, the estimated source position is taken into account to remove the source geometric phase. After this step, the phase becomes $\phi_o = 2\pi\nu_o \frac{B \cdot (S_o - S_e)}{c}$, where S_o is the true source position, and

S_c is the estimated source position used in data cross-correlation. For VLBI observations of masers, the phase of a target maser spot at frequency $\nu = \nu_o + \Delta\nu$ is:

$$\begin{aligned}\phi &= 2\pi\nu \frac{B \cdot (S_o - S_c + S)}{c} \\ &= 2\pi(\nu_o + \Delta\nu) \frac{B \cdot (S_o - S_c + S)}{c}\end{aligned}$$

where S is the projected position difference between the maser spot at frequency ν and the reference position S_o .

Subtracting the phase corresponding to the reference position from the phase of a given maser spot, we got the relative phase difference $\Delta\phi$, which is what we actually measured. $\Delta\phi$ is given by:

$$\begin{aligned}\Delta\phi &= \phi - \phi_o \\ &= 2\pi(\nu_o + \Delta\nu) \frac{B \cdot (S_o - S_c + S)}{c} - 2\pi\nu_o \frac{B \cdot S}{c} \\ &= 2\pi \frac{B}{c} [(\nu_o + \Delta\nu)(S_o - S_c + S) - \nu_o(S_o - S_c)] \\ &= 2\pi \frac{B}{c} [\nu_o S + \Delta\nu(S_o - S_c + S)]\end{aligned}$$

The second term in the bracket contains the additional phase caused by absolute source position uncertainty $\Delta\nu(S_o - S_c)$. To neglect this term's effect would require $\frac{\nu_o S}{\Delta\nu(S_o - S_c + S)} \gg 1$.

For NGC 5765b, the frequency for the reference feature is $\nu_o = 21636$ MHz, and all high-velocity features are within 64 MHz of the reference feature. Based on our initial VLBI map, the position difference of the high-velocity features and the reference feature in the systemic part is greater than 0.3 mas. Putting these numbers in the equation above, if we require the additional phase to be less than 1/10 of the original phase, we have $(S_o - S_c + S) \sim (S_o - S_c) \leq 10$ mas, so the absolute source position uncertainty should be within 10 mas.

For other maser targets, the required position accuracy depends on the maser frequency coverage and the size of the maser disk. For targets in the MCP, 10 mas is usually sufficient.

B. Derivation of the relation between maser intensity and radius on the disk

Suppose maser clouds are located on the disk with position (r, ϕ) , in which ϕ is measured relative to the LOS direction, and on the midline red-shifted masers have $\phi = +90$, while

blue-shifted masers have $\phi = -90$. For an arbitrary maser cloud, the LOS velocity is given by $V_1 = V_r \cdot \cos(90 - \phi_1)$, where V_r is the Keplerian rotation velocity defined by $V_r = \sqrt{GM/r}$. For another masing cloud located at $(r, \phi_2 = \phi_1 + \Delta\phi)$, the LOS velocity is given by $V_2 = V_r \cdot \cos(90 - \phi_1 - \Delta\phi)$. Maintaining the velocity coherence required for maser amplification would require $\Delta V = V_2 - V_1 \leq 1 \text{ km s}^{-1}$. If $\Delta\phi$ is infinitesimal, ΔV can be written as $\Delta V = \sqrt{GM/r} \cdot \cos(\phi_1) \cdot \Delta\phi \leq 1 \text{ km s}^{-1}$.

For the same maser clouds, we define the gain length as the position difference projected on the LOS direction $\Delta L = r \cdot (\cos\phi_2 - \cos\phi_1) = r \cdot \sin(\phi_1) \cdot \Delta\phi$. If we assume maser emission could be generated and amplified through the two maser clouds along the LOS direction and the maser intensity is proportional to the gain length by multiplying a constant, g , then the maser flux is $F = g \cdot \Delta L = g \cdot r \cdot \sin(\phi_1) \cdot \Delta\phi$. Replacing $\Delta\phi$ from above, finally we have $F = g \cdot r \cdot \sin(\phi_1) \cdot \Delta\phi = g \cdot \tan(\phi_1) \cdot r^{1.5} / \sqrt{GM}$.

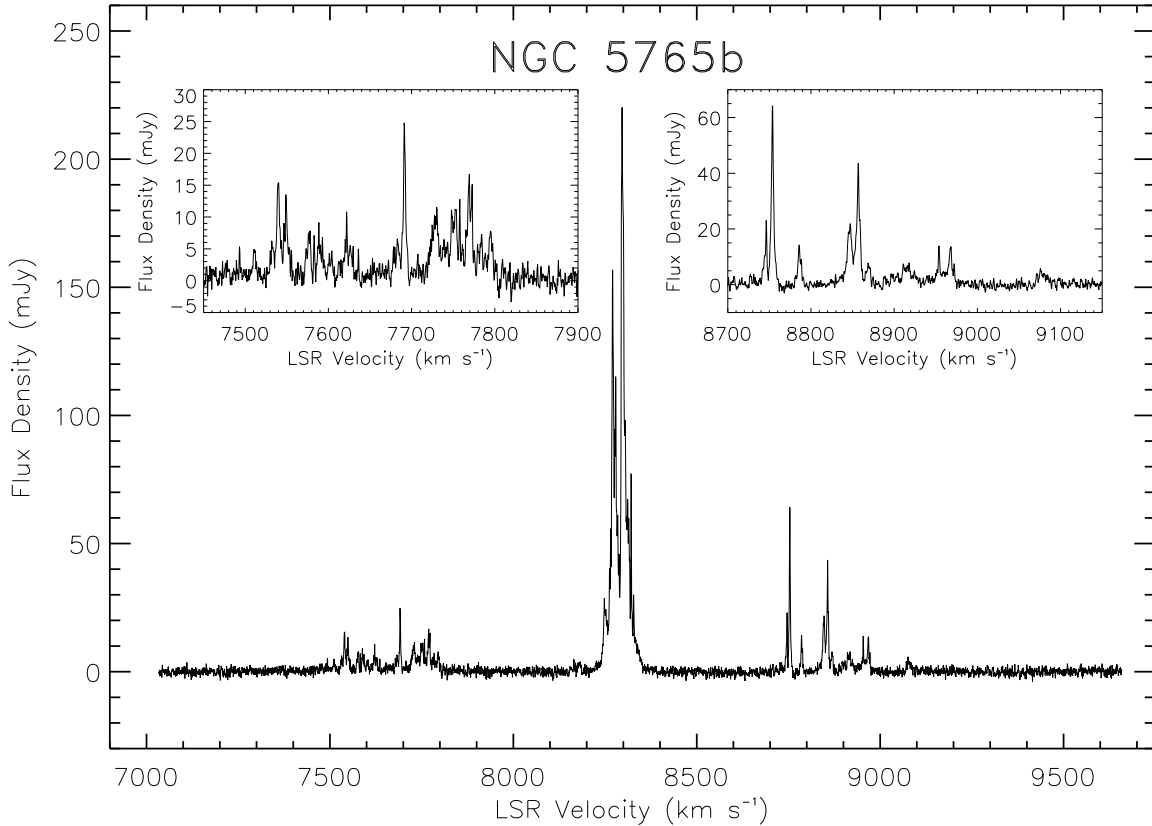


Fig. 1.— A representative spectrum of the 22 GHz water maser in NGC 5765b, observed on 2014 April 06 by the GBT. The LSR recession velocity of the galaxy is 8345 km s^{-1} , as obtained from NED. The two insets show zoomed-in details of the high-velocity masers.

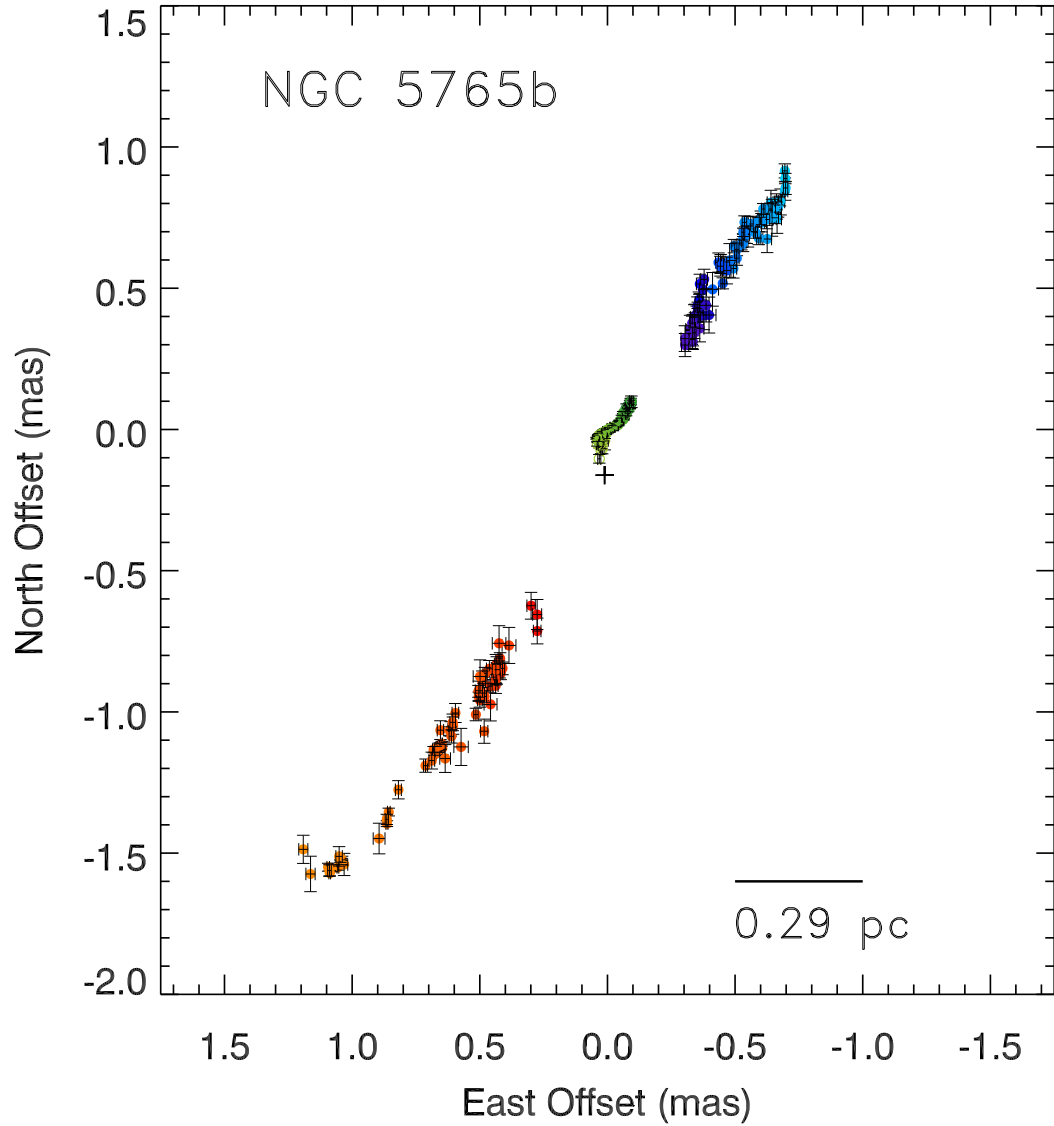


Fig. 2.— The combined VLBI map with a flux cutoff of 3 mJy, which is at the 10σ level. The maser positions are referenced to the strongest systemic feature at $8295.91 \text{ km s}^{-1}$, with the black cross marking the dynamic center derived from the fitting of the rotation curve, as shown in Fig. 3. The horizontal bar in the lower right corner marks the corresponding physical size, using a nominal distance of 119 Mpc to NGC 5765b.

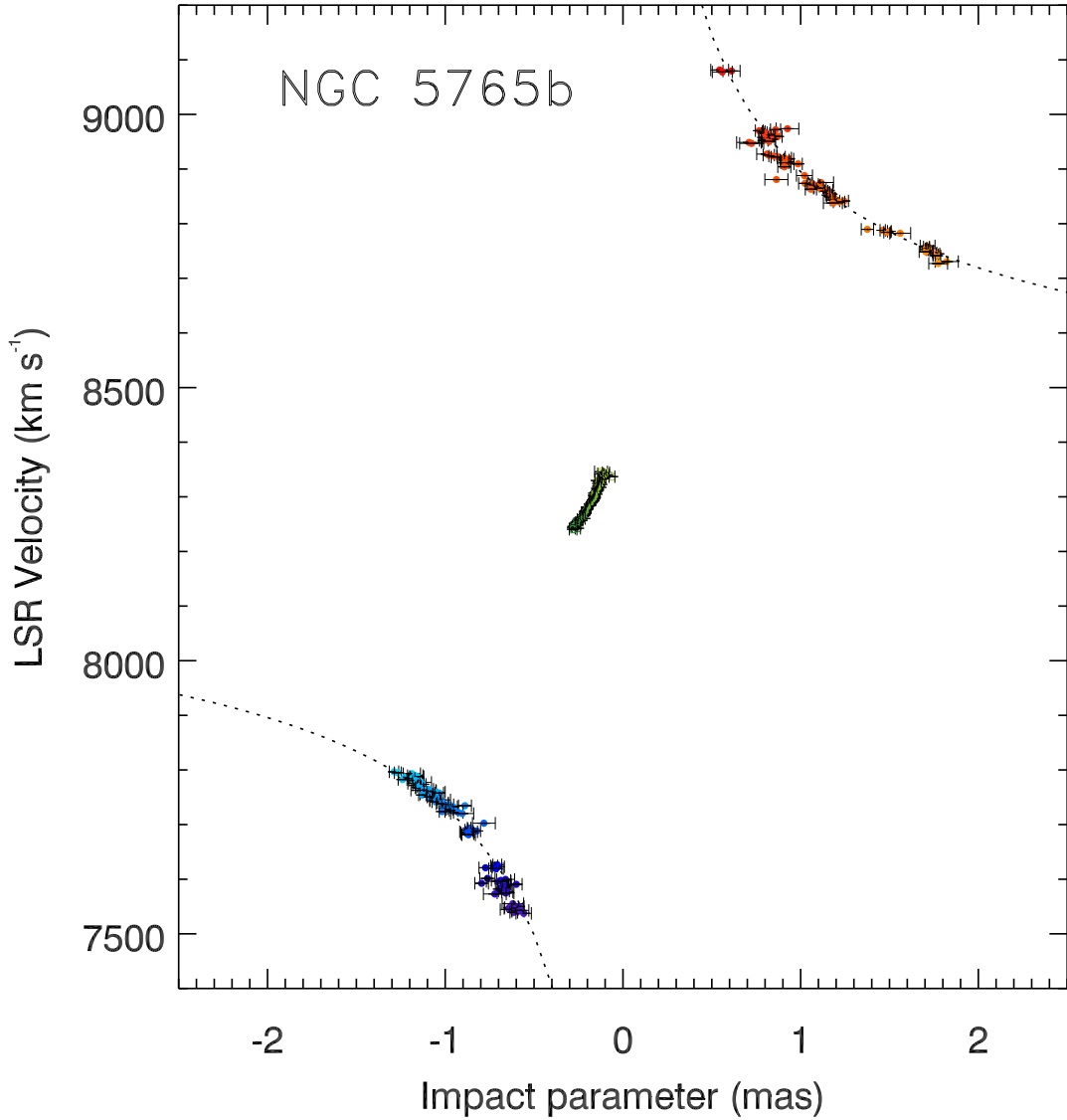


Fig. 3.— The position-velocity diagram from the combined VLBI results, with a flux cutoff of 3 mJy, which is at the 10σ level. The dotted line shows the best-fit Keplerian rotation curve assuming an edge-on thin disk model without disk warping. This model gives an enclosed mass of $4.4 \pm 0.44 \times 10^7 M_\odot$ and a recession velocity of 8304 km s^{-1} . The origin on the X-axis marks the position of the dynamic center. For most of the high-velocity features, their deviation from the fitted rotation curve is less than 5% of their rotation velocity.

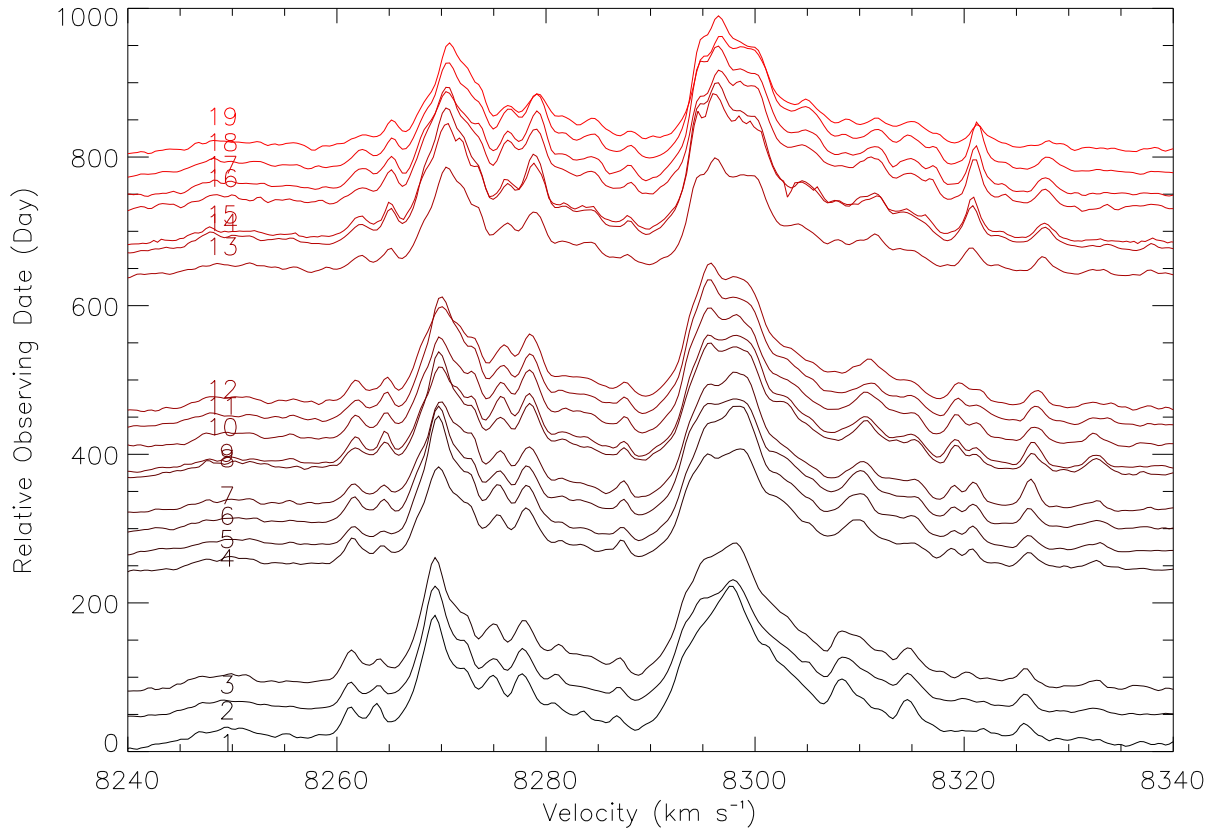


Fig. 4.— Stacked spectra from GBT monitoring data, zoomed on the systemic part, with the date referenced to 2012 February 26. Data from epoch 15 comes from VLBI tracks BB321T Y2 Y3 and Y4 combined, as a complement to the unscheduled GBT monitoring observation.

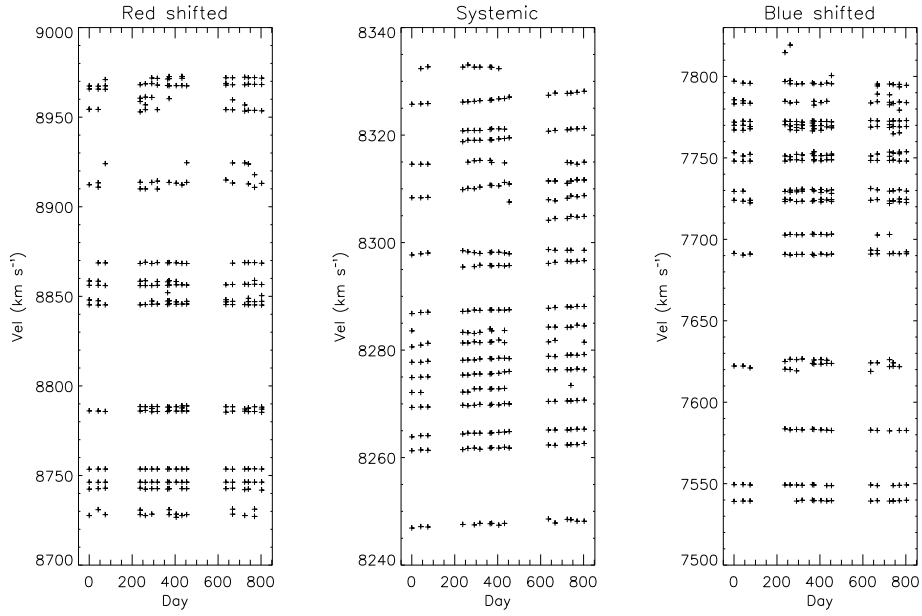


Fig. 5.— These acceleration plots show velocities of the maser line peaks in both the systemic and high-velocity parts. Each cross marks a peak velocity at the given epoch, identified by eye. The date on the X-axis is referenced to the first GBT monitoring observation data, 2012 February 26. The “negative” slope seen in several systemic features (e.g. ~ 8300 km s⁻¹ in the middle epochs) appears to result from lines blending together and the emerging of new peaks at adjacent velocities. This is better illustrated in Fig. 4.

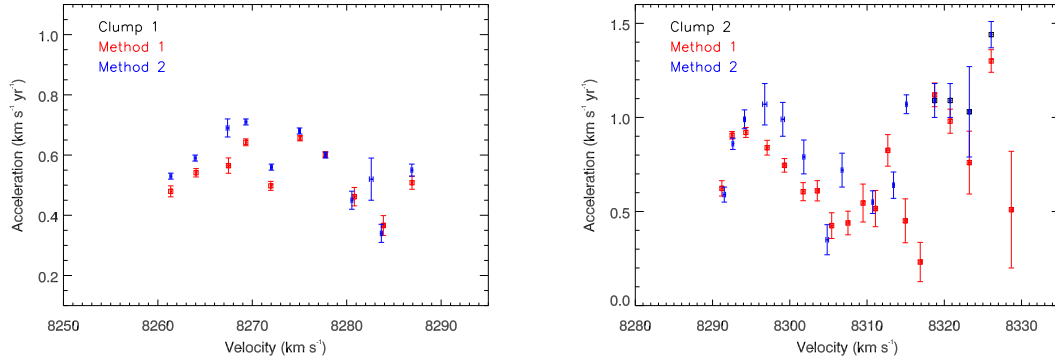


Fig. 6.— Comparison of the acceleration results between method 1 and method 2, for both clump 1 and clump 2 in the systemic part.

Table 1. VLBI Observation Details

Project Code	Date	Antennas	Synthesized Beam (mas x mas, deg)	Track Length hour	Sensitivity mJy	Observing Mode
BB313 J	2012 Apr 14	VLBA+GB+EB	1.04 x 0.27,-10.49	10	1.10	Self-cal.
BB313 AC	2012 Nov 09	VLBA+GB+EB	1.00 x 0.26,-11.94	12	1.25	Phase-ref.
BB321 C	2013 Feb 16	VLBA+Y	1.42 x 0.47,-16.66	6	0.72	Self-cal.
BB321 E1	2013 Feb 17	VLBA+Y	1.37 x 0.40,-18.05	7	0.78	Self-cal.
BB321 F	2013 Feb 21	VLBA+Y	1.97 x 0.56,-16.08	6.25	0.93	Self-cal.
BB321 L	2013 Mar 13	VLBA+GB+Y	—————	7	—————	Self-cal.
BB321 N	2013 Mar 14	VLBA+GB+Y	1.90 x 0.49,-6.68	5	0.59	Self-cal.
BB321 S	2013 Apr 13	VLBA+GB+Y	—————	7	—————	Self-cal.
BB321 T	2013 Dec 03	VLBA+GB+Y	1.00 x 0.32, -8.93	6	0.83	Self-cal.
BB321 Y2	2014 Jan 12	VLBA+GB+Y	1.49 x 0.36,-14.00	6	0.52	Self-cal.
BB321 Y3	2014 Jan 13	VLBA+GB+Y	1.52 x 0.38,-12.33	6	0.53	Self-cal.
BB321 Y4	2014 Jan 16	VLBA+GB+Y	1.51 x 0.41,-9.55	6	0.42	Self-cal.
BB321 Y5	2014 Jan 17	VLBA	0.69 x 0.23,-13.19	6	2.00	Phase-ref.

Note. — VLBI observation details. Data for BB321L and BB321S were affected by bad weather and instrument problems, so we didn't make the VLBI map from these 2 tracks.

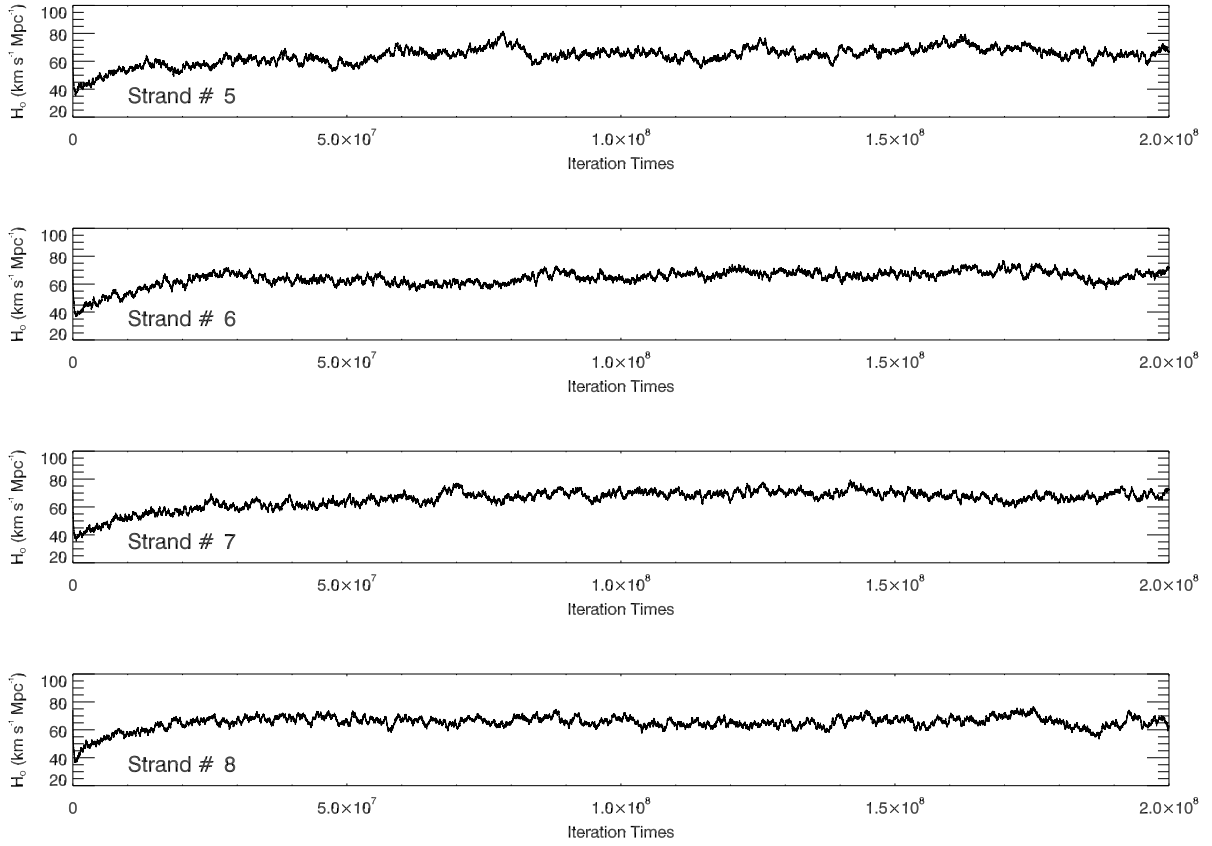


Fig. 7.— Example of the H_0 versus iteration number plot for several strands in our fit. Note that H_0 starts from an initial value between 60 and 80, then quickly drops to ~ 40 at the very beginning iterations, then gradually converges to the final result. In our calculation of the posteriori probability distribution function, we discard records from the first 20% of the iterations to avoid unconverged trials in our final result.

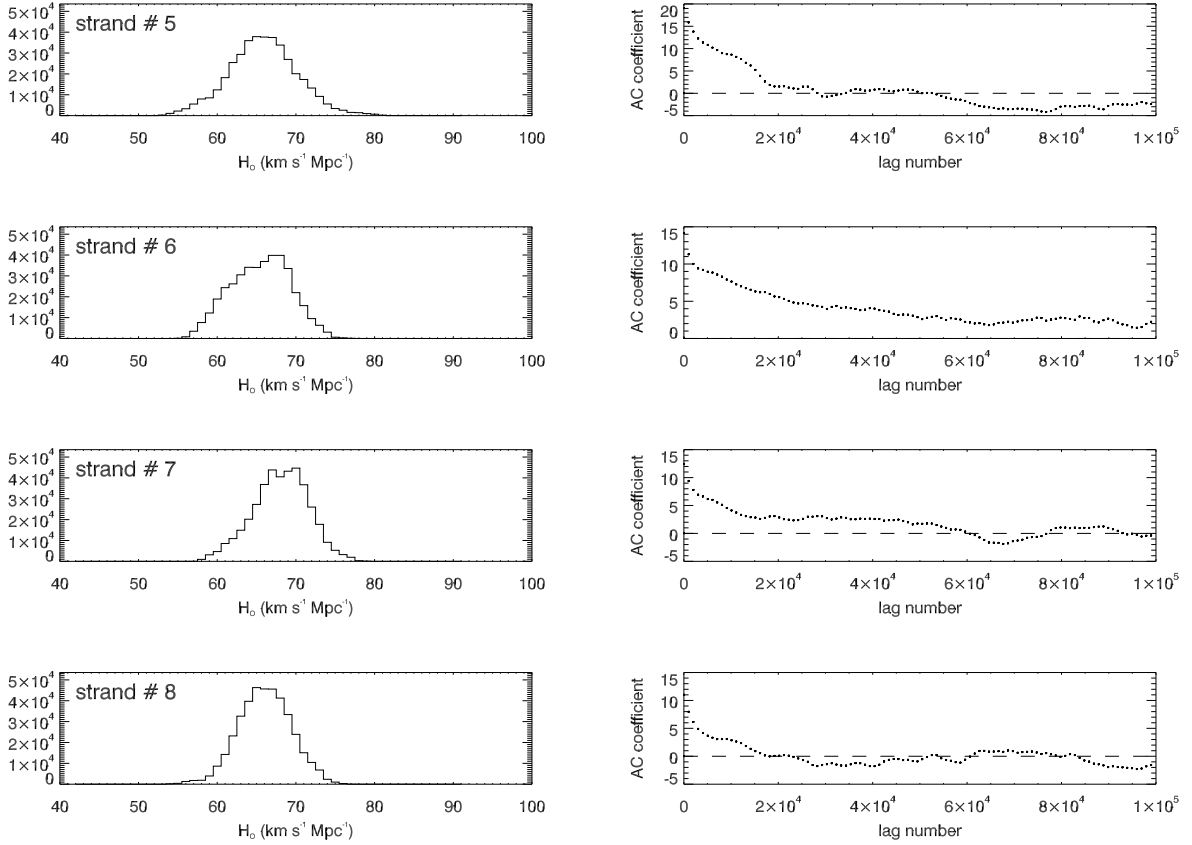


Fig. 8.— Example of the probability distribution of H_0 and the auto-correlation (AC) function versus lag number for several strands. The AC functions are used to check for fitting convergence. We require the AC function to drop to near zero before 40% of the maximum lag number. The maximum lag number is defined as 25% of the total number of recorded MCMC trials in each strand. In our case, we record every 400th record of the total 2×10^8 trials, after discarding the first 20%, so the maximum lag number is 1×10^5 . Here strand 6 is not quite converged according to our criteria. Usually if 6 or 7 out of the total 10 strands are converged, we consider the total fitting result as converged.

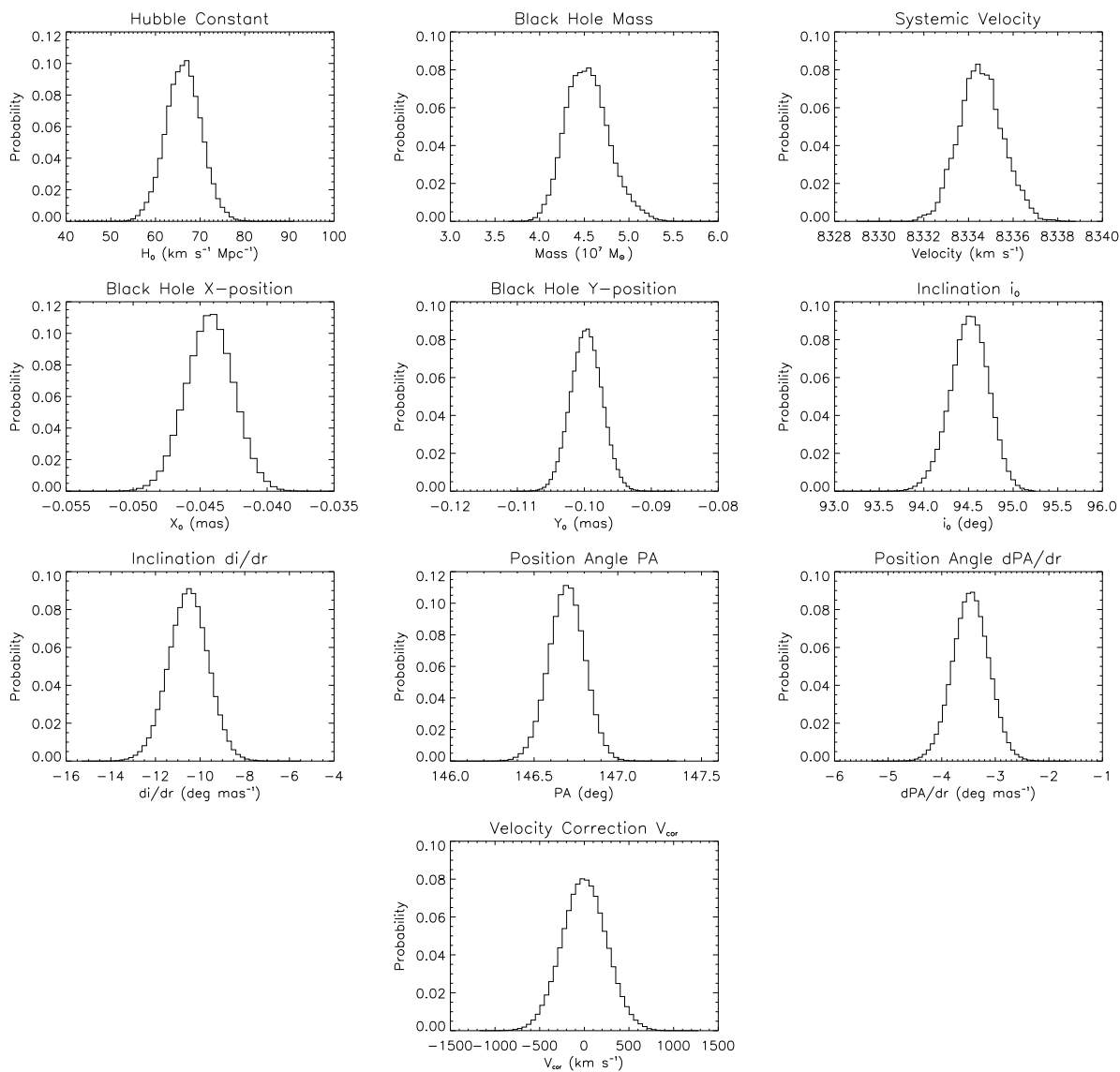


Fig. 9.— Combined posteriori probability distributions for the global disk parameters describing the disk model for all 10 strands.

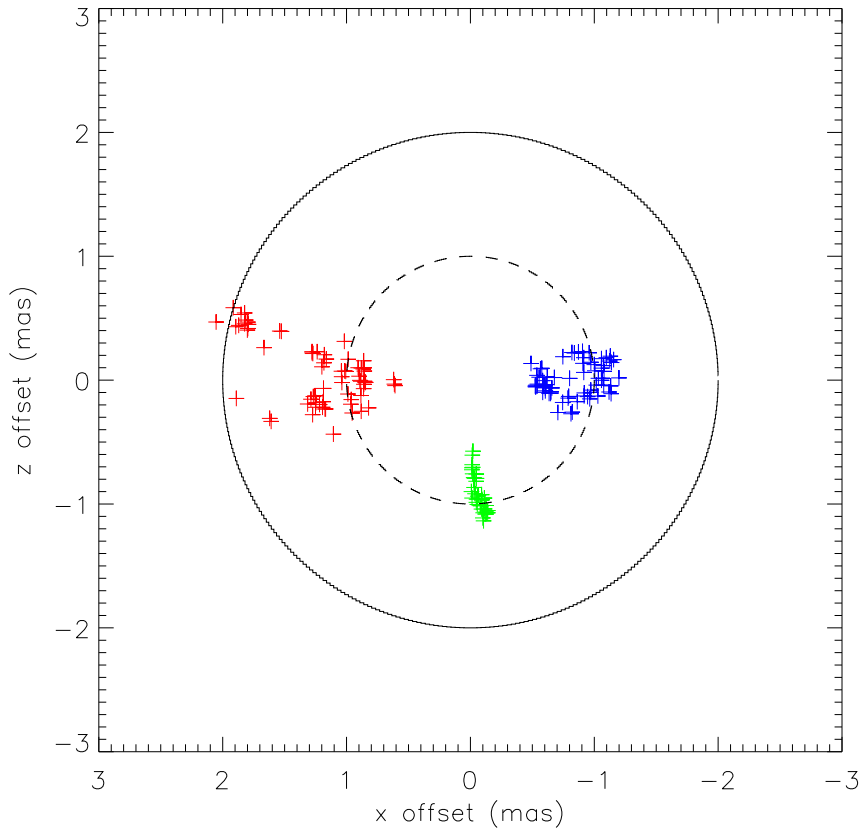


Fig. 10.— Model-fitted position distribution of the maser spots viewed on the disk plane. The red, green and blue colors represent the red-shifted, systemic and blue-shifted masers, respectively. For the high-velocity features (especially the red-shifted features), maser spots are clustered into several clumps on the disk. This is different from the case of NGC 4258 where the high-velocity masers are seen to be radially localized (as shown in Humphreys et al. 2013).

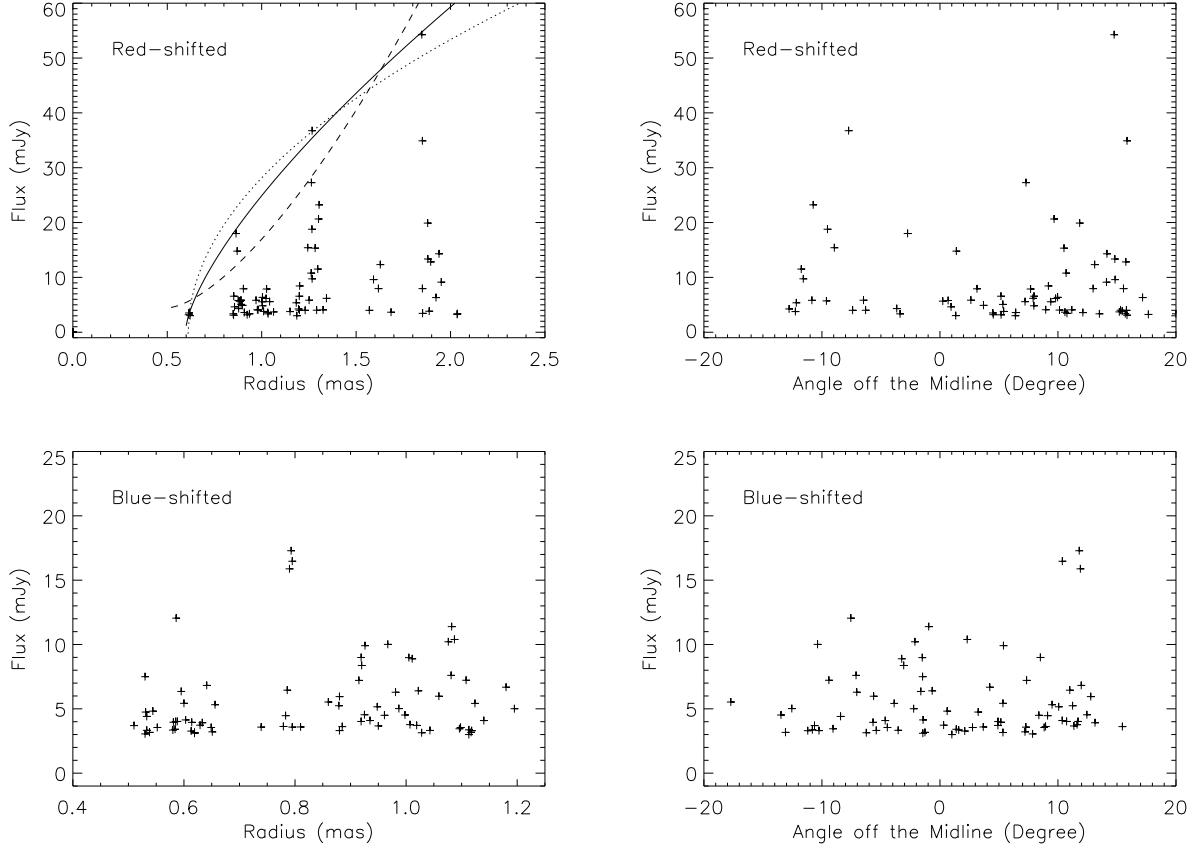


Fig. 11.— Modeled radius and angle versus peak intensity for the high-velocity masers in NGC 5765b. The upper left plot shows the radius versus peak intensity for the red-shifted features, and the solid line shows the best fit to the outline of the maser line peaks, with $\text{flux} \propto r^{0.7}$. For comparison, the dotted line has $\text{flux} \propto r^{0.5}$, while the dashed line has $\text{flux} \propto r^{1.5}$. The upper right panel shows the angle off the midline versus maser peak intensity for the red-shifted features. The maser peaks appear away from the midline. Plots for the blue-shifted features are on the bottom panel. The blue-shifted features show no such dependencies as seen in the red-shifted features.

Table 2. VLBI position for NGC 5765b and the phase-reference calibrators

Name	Right Ascension	Declination	uncertainty in R.A. (mas)	Uncertainty in DEC. (mas)
J1448+0402	$14^h48^m50^s.361110$	$+04^\circ02'19''.89244$	1.68	2.05
J1458+0416	$14^h58^m59^s.356215$	$+04^\circ16'13''.82056$	0.03	0.05
NGC 5765b	$14^h50^m51^s.51950$	$+05^\circ06'52''.2502$	0.1	0.7

Note. — Positions for J1448+0402 and J1458+0416 are from the VLBA Calibrator Survey. Position for NGC 5765b is measured in reference to J1458+0416.

Table 3. GBT Monitoring Observation Details

Epoch	Date Observed	Day Number	Tsys (K)	rms noise (mJy)
1	2012 Feb 26	0	53.0	1.93
2	2012 Apr 08	42	40.0	1.23
3	2012 May 11	75	48.3	1.38
4	2012 Oct 20	237	48.9	1.33
5	2012 Nov 13	261	36.2	1.15
6	2012 Dec 13	291	35.7	1.07
7	2013 Jan 08	317	38.5	1.18
8	2013 Feb 25	365	35.4	1.71
9	2013 Mar 04	372	39.1	1.21
10	2013 Apr 06	405	46.1	1.38
11	2013 May 03	432	42.4	1.17
12	2013 May 25	454	41.1	1.38
13	2013 Nov 23	636	46.4	1.65
14	2013 Dec 24	667	45.0	1.38
15*	2014 Jan 03	677	—	1.29
16	2014 Feb 09	724	63.5	2.18
17	2013 Mar 08	741	53.5	1.64
18	2014 Apr 06	770	38.0	1.05
19	2014 May 09	803	60.9	1.69

Note. — *Due to the lack of a GBT observation, here we use the spectrum from the combined VLBI data of BB321T Y2 Y3 & Y4.

Table 4. Acceleration Measurements for the Systemic Masers from Method 1

Velocity km s ⁻¹	Epochs	Line width km s ⁻¹	Acceleration km s ⁻¹ yr ⁻¹	A _σ km s ⁻¹ yr ⁻¹
8261.36	1-19	2.52	0.48	0.018
8264.05	1-19	2.02	0.54	0.014
8267.48	1-19	3.14	0.57	0.025
8269.31	1-19	2.25	0.64	0.011
8271.96	1-19	3.49	0.50	0.015
8275.06	1-19	2.08	0.66	0.009
8277.74	1-19	2.55	0.60	0.010
8280.81	1-19	2.97	0.46	0.031
8283.88	1-19	3.24	0.37	0.033
8286.92	1-19	2.43	0.51	0.022
8291.61	4-19	3.33	0.62	0.041
8293.12	4-19	1.72	0.91	0.020
8294.91	4-19	2.75	0.92	0.026
8297.61	4-19	3.05	0.84	0.039
8299.79	4-19	2.46	0.75	0.036
8302.12	4-19	2.37	0.61	0.048
8303.95	4-19	2.05	0.61	0.054
8305.70	4-19	2.09	0.43	0.068
8307.81	4-19	2.41	0.44	0.063
8309.84	4-19	2.33	0.55	0.101
8311.42	4-19	2.30	0.52	0.096
8313.23	4-19	2.25	0.82	0.084
8315.25	4-19	2.15	0.45	0.117
8317.04	4-19	2.02	0.23	0.104
8318.75	4-12	1.81	1.12	0.063
8320.76	4-12	1.83	0.98	0.064
8323.24	4-12	2.98	0.76	0.167
8326.08	4-12	1.92	1.30	0.060
8328.69	4-12	3.04	0.52	0.310

Table 5. Acceleration Measurement for the High Velocity Masers from the “by eye” method

Velocity km s ⁻¹	Acceleration km s ⁻¹ yr ⁻¹	A _σ km s ⁻¹ yr ⁻¹
7539.46	0.100	0.074
7549.10	-0.175	0.066
7582.95	-0.528	0.110
7690.85	0.222	0.110
7702.90	0.006	0.157
7723.64	0.007	0.215
7729.82	0.269	0.252
7748.40	0.088	0.129
7769.05	0.458	0.679
7772.26	-0.038	0.255
7795.54	0.282	0.567
8727.88	-0.159	0.250
8730.99	0.199	0.095
8742.55	-0.186	0.101
8746.26	0.015	0.012
8753.59	0.034	0.018
8788.41	-0.047	0.022
8845.42	-0.007	0.078
8847.21	-0.215	0.059
8856.32	0.330	0.046
8858.49	0.121	0.148
8868.63	0.034	0.088
8924.27	0.060	0.238
8954.25	-0.102	0.031
8967.54	0.123	0.113
8968.26	0.007	0.691
8972.02	-0.285	0.432

Table 6. Input Data for the Disk Fitting Program

Velocity km s ⁻¹	X mas	X _σ mas	Y mas	Y _σ mas	A km s ⁻¹ yr ⁻¹	A _σ km s ⁻¹ yr ⁻¹
8345.76	0.009	0.0143	-0.026	0.0334	1.000	1.000
8344.03	0.019	0.0071	-0.055	0.0188	1.000	1.000
8342.25	0.026	0.0056	-0.025	0.0152	1.000	1.000
8340.47	0.023	0.0048	-0.060	0.0129	1.000	1.000
8338.69	0.023	0.0042	-0.044	0.0115	1.000	1.000
8336.90	0.030	0.0060	-0.091	0.0153	1.000	1.000
8335.12	0.028	0.0047	-0.041	0.0125	1.000	1.000
8333.34	0.038	0.0029	-0.039	0.0073	1.000	1.000
8331.56	0.029	0.0032	-0.027	0.0080	1.000	1.000
8329.78	0.012	0.0036	-0.003	0.0099	0.520	0.310
8327.99	0.009	0.0019	-0.014	0.0052	0.520	0.310
8326.21	0.014	0.0020	-0.023	0.0051	1.300	0.152
8324.43	0.023	0.0029	-0.012	0.0078	0.760	0.318
8322.65	0.033	0.0020	-0.029	0.0055	0.760	0.318
8320.86	0.041	0.0012	-0.019	0.0032	0.980	0.127
8319.08	0.035	0.0016	-0.014	0.0040	1.120	0.070
8317.30	0.037	0.0017	-0.025	0.0047	0.230	0.846
8315.52	0.034	0.0012	-0.008	0.0032	0.450	0.223
8313.73	0.030	0.0011	-0.010	0.0030	0.820	0.199
8311.95	0.032	0.0011	-0.009	0.0029	0.520	0.067
8310.17	0.029	0.0010	-0.004	0.0027	0.550	0.697
8308.39	0.016	0.0011	0.003	0.0029	0.440	0.287
8306.61	0.000	0.0010	0.011	0.0028	0.430	0.105
8304.82	0.000	0.0009	0.000	0.0025	0.610	0.186
8303.04	-0.002	0.0011	0.012	0.0028	0.610	0.186
8301.26	-0.002	0.0008	0.010	0.0021	0.750	0.243
8299.48	-0.003	0.0007	0.009	0.0019	0.750	0.243
8297.69	-0.002	0.0007	0.010	0.0019	0.840	0.233
8295.91	-0.002	0.0007	0.013	0.0020	0.920	0.075
8294.13	-0.012	0.0008	0.018	0.0021	0.920	0.075

Table 6—Continued

Velocity km s ⁻¹	X mas	X _σ mas	Y mas	Y _σ mas	A km s ⁻¹ yr ⁻¹	A _σ km s ⁻¹ yr ⁻¹
8292.35	-0.016	0.0010	0.016	0.0027	0.620	0.065
8290.56	-0.024	0.0015	0.021	0.0039	0.620	0.065
8288.78	-0.031	0.0016	0.023	0.0042	0.510	0.046
8287.00	-0.037	0.0013	0.030	0.0034	0.510	0.046
8285.22	-0.040	0.0014	0.029	0.0036	0.370	0.045
8283.44	-0.044	0.0010	0.029	0.0028	0.370	0.045
8281.65	-0.049	0.0010	0.043	0.0027	0.460	0.033
8279.87	-0.053	0.0009	0.042	0.0024	0.600	0.010
8278.09	-0.052	0.0008	0.041	0.0022	0.600	0.010
8276.31	-0.056	0.0009	0.043	0.0024	0.660	0.022
8274.53	-0.060	0.0009	0.048	0.0024	0.500	0.062
8272.74	-0.062	0.0008	0.049	0.0022	0.500	0.062
8270.96	-0.063	0.0008	0.048	0.0022	0.500	0.062
8269.18	-0.065	0.0008	0.049	0.0021	0.640	0.071
8267.40	-0.064	0.0010	0.056	0.0025	0.570	0.123
8265.61	-0.065	0.0012	0.057	0.0033	0.540	0.052
8263.83	-0.064	0.0013	0.065	0.0034	0.540	0.052
8262.05	-0.063	0.0013	0.073	0.0034	0.480	0.053
8260.27	-0.058	0.0020	0.058	0.0051	0.480	0.053
8258.48	-0.078	0.0028	0.084	0.0074	1.000	1.000
8256.70	-0.075	0.0028	0.069	0.0075	1.000	1.000
8254.92	-0.083	0.0025	0.082	0.0065	1.000	1.000
8253.14	-0.088	0.0024	0.091	0.0065	1.000	1.000
8251.36	-0.089	0.0020	0.102	0.0053	1.000	1.000
8249.57	-0.086	0.0021	0.091	0.0056	1.000	1.000
8247.79	-0.090	0.0019	0.092	0.0053	1.000	1.000
8246.01	-0.090	0.0027	0.109	0.0074	1.000	1.000
8244.23	-0.093	0.0042	0.112	0.0116	1.000	1.000
8242.44	-0.077	0.0051	0.089	0.0140	1.000	1.000
8240.66	-0.095	0.0075	0.111	0.0204	1.000	1.000

Table 6—Continued

Velocity km s ⁻¹	X mas	X _σ mas	Y mas	Y _σ mas	A km s ⁻¹ yr ⁻¹	A _σ km s ⁻¹ yr ⁻¹
9081.29	0.297	0.0163	-0.611	0.0474	0.000	0.200
9079.50	0.273	0.0150	-0.701	0.0457	0.000	0.200
9077.71	0.274	0.0176	-0.642	0.0533	0.000	0.200
8973.79	0.456	0.0253	-0.960	0.0589	0.000	0.200
8972.08	0.436	0.0100	-0.895	0.0300	-0.285	0.476
8970.29	0.419	0.0100	-0.798	0.0300	0.000	0.200
8968.50	0.431	0.0100	-0.820	0.0300	0.007	0.719
8966.71	0.422	0.0100	-0.837	0.0300	0.123	0.230
8964.92	0.429	0.0100	-0.835	0.0300	0.000	0.200
8963.13	0.437	0.0104	-0.853	0.0300	0.000	0.200
8961.35	0.417	0.0100	-0.851	0.0300	0.000	0.200
8959.56	0.458	0.0100	-0.897	0.0300	0.000	0.200
8957.77	0.432	0.0100	-0.817	0.0300	0.000	0.200
8955.98	0.421	0.0100	-0.841	0.0300	0.000	0.200
8954.19	0.435	0.0100	-0.871	0.0300	-0.102	0.202
8952.40	0.409	0.0100	-0.833	0.0300	0.000	0.200
8950.61	0.432	0.0137	-0.854	0.0353	0.000	0.200
8948.75	0.384	0.0272	-0.752	0.0637	0.000	0.200
8946.97	0.423	0.0266	-0.744	0.0622	0.000	0.200
8927.43	0.435	0.0164	-0.838	0.0541	0.000	0.200
8925.57	0.461	0.0114	-0.835	0.0300	0.000	0.200
8923.78	0.478	0.0100	-0.851	0.0300	0.060	0.311
8921.99	0.488	0.0128	-0.880	0.0378	0.000	0.200
8920.21	0.483	0.0138	-0.924	0.0373	0.000	0.200
8918.42	0.498	0.0100	-0.945	0.0300	0.000	0.200
8916.63	0.488	0.0100	-0.924	0.0300	0.000	0.200
8914.84	0.480	0.0100	-0.933	0.0300	0.000	0.200
8913.05	0.502	0.0100	-0.933	0.0300	0.000	0.200
8911.26	0.504	0.0100	-0.914	0.0300	0.000	0.200
8909.47	0.514	0.0100	-0.996	0.0300	0.000	0.200

Table 6—Continued

Velocity km s ⁻¹	X mas	X _σ mas	Y mas	Y _σ mas	A km s ⁻¹ yr ⁻¹	A _σ km s ⁻¹ yr ⁻¹
8904.11	0.502	0.0139	-0.912	0.0340	0.000	0.200
8888.07	0.481	0.0143	-1.056	0.0428	0.000	0.200
8880.79	0.497	0.0270	-0.862	0.0588	0.000	0.200
8875.43	0.572	0.0281	-1.111	0.0657	0.000	0.200
8873.70	0.594	0.0131	-0.991	0.0337	0.000	0.200
8871.91	0.603	0.0118	-1.036	0.0306	0.000	0.200
8870.12	0.612	0.0106	-1.048	0.0300	0.000	0.200
8868.33	0.615	0.0100	-1.055	0.0300	0.034	0.219
8866.54	0.609	0.0100	-1.074	0.0300	0.000	0.200
8864.75	0.653	0.0124	-1.052	0.0331	0.000	0.200
8862.96	0.604	0.0110	-1.024	0.0300	0.000	0.200
8861.17	0.646	0.0100	-1.116	0.0300	0.000	0.200
8859.39	0.648	0.0100	-1.100	0.0300	0.121	0.249
8857.60	0.654	0.0100	-1.110	0.0300	0.121	0.249
8855.81	0.658	0.0100	-1.108	0.0300	0.330	0.205
8854.02	0.662	0.0100	-1.123	0.0300	0.000	0.200
8852.23	0.652	0.0100	-1.108	0.0300	0.000	0.200
8850.44	0.660	0.0100	-1.111	0.0300	0.000	0.200
8848.65	0.670	0.0100	-1.118	0.0300	0.000	0.200
8846.87	0.672	0.0100	-1.136	0.0300	-0.215	0.209
8845.08	0.675	0.0100	-1.135	0.0300	-0.007	0.215
8843.29	0.679	0.0100	-1.121	0.0300	0.000	0.200
8841.50	0.711	0.0100	-1.178	0.0300	0.000	0.200
8839.71	0.686	0.0115	-1.160	0.0300	0.000	0.200
8837.87	0.634	0.0210	-1.152	0.0492	0.000	0.200
8789.62	0.817	0.0118	-1.263	0.0324	0.000	0.200
8787.84	0.855	0.0100	-1.342	0.0300	-0.047	0.201
8786.05	0.862	0.0100	-1.383	0.0300	0.000	0.200
8784.26	0.863	0.0100	-1.368	0.0300	0.000	0.200
8782.43	0.893	0.0231	-1.436	0.0541	0.000	0.200

Table 6—Continued

Velocity km s ⁻¹	X mas	X _σ mas	Y mas	Y _σ mas	A km s ⁻¹ yr ⁻¹	A _σ km s ⁻¹ yr ⁻¹
8759.21	1.030	0.0140	-1.527	0.0393	0.000	0.200
8757.43	1.038	0.0100	-1.514	0.0300	0.000	0.200
8755.64	1.043	0.0100	-1.521	0.0300	0.000	0.200
8753.85	1.040	0.0100	-1.509	0.0300	0.034	0.201
8752.06	1.044	0.0100	-1.516	0.0300	0.000	0.200
8750.27	1.054	0.0100	-1.538	0.0300	0.000	0.200
8748.48	1.049	0.0126	-1.499	0.0345	0.000	0.200
8746.69	1.078	0.0100	-1.543	0.0300	0.015	0.200
8744.90	1.086	0.0100	-1.558	0.0300	0.000	0.200
8743.12	1.092	0.0100	-1.537	0.0300	-0.186	0.224
8741.33	1.087	0.0100	-1.549	0.0300	0.000	0.200
8730.62	1.161	0.0182	-1.561	0.0627	0.199	0.221
8727.04	1.190	0.0177	-1.474	0.0499	-0.159	0.320
7796.67	-0.697	0.0100	0.928	0.0300	0.282	0.601
7794.89	-0.698	0.0100	0.901	0.0300	0.282	0.601
7793.12	-0.680	0.0160	0.818	0.0460	0.000	0.200
7789.57	-0.664	0.0151	0.806	0.0409	0.000	0.200
7787.79	-0.665	0.0154	0.794	0.0368	0.000	0.200
7786.02	-0.697	0.0108	0.857	0.0325	0.000	0.200
7784.24	-0.678	0.0100	0.821	0.0300	0.000	0.200
7782.47	-0.699	0.0100	0.868	0.0300	0.000	0.200
7780.69	-0.670	0.0132	0.800	0.0354	0.000	0.200
7777.21	-0.666	0.0174	0.757	0.0505	0.000	0.200
7775.43	-0.642	0.0147	0.816	0.0433	0.000	0.200
7773.59	-0.657	0.0100	0.758	0.0300	0.000	0.200
7771.82	-0.664	0.0100	0.804	0.0300	-0.038	0.324
7770.04	-0.652	0.0100	0.788	0.0300	0.000	0.200
7768.27	-0.656	0.0100	0.795	0.0300	0.458	0.708
7766.49	-0.639	0.0100	0.794	0.0300	0.000	0.200
7764.72	-0.602	0.0106	0.759	0.0300	0.000	0.200

Table 6—Continued

Velocity km s ⁻¹	X mas	X _σ mas	Y mas	Y _σ mas	A km s ⁻¹ yr ⁻¹	A _σ km s ⁻¹ yr ⁻¹
7762.88	-0.646	0.0254	0.762	0.0654	0.000	0.200
7761.17	-0.605	0.0127	0.745	0.0324	0.000	0.200
7759.45	-0.627	0.0172	0.687	0.0483	0.000	0.200
7757.62	-0.595	0.0100	0.690	0.0300	0.000	0.200
7755.84	-0.625	0.0124	0.756	0.0328	0.000	0.200
7754.07	-0.612	0.0100	0.794	0.0300	0.000	0.200
7752.29	-0.592	0.0100	0.749	0.0300	0.000	0.200
7750.52	-0.601	0.0100	0.751	0.0300	0.000	0.200
7748.74	-0.576	0.0100	0.719	0.0300	0.088	0.238
7746.97	-0.582	0.0100	0.710	0.0300	0.000	0.200
7745.14	-0.552	0.0230	0.712	0.0538	0.000	0.200
7743.42	-0.563	0.0100	0.740	0.0300	0.000	0.200
7741.64	-0.538	0.0100	0.746	0.0300	0.000	0.200
7739.87	-0.541	0.0104	0.701	0.0300	0.000	0.200
7738.09	-0.547	0.0113	0.702	0.0313	0.000	0.200
7736.32	-0.533	0.0116	0.674	0.0316	0.000	0.200
7734.54	-0.495	0.0131	0.583	0.0341	0.000	0.200
7732.77	-0.497	0.0100	0.662	0.0300	0.000	0.200
7730.99	-0.529	0.0100	0.672	0.0300	0.000	0.200
7729.22	-0.534	0.0100	0.690	0.0300	0.269	0.322
7727.44	-0.526	0.0100	0.666	0.0300	0.000	0.200
7725.67	-0.509	0.0100	0.650	0.0300	0.000	0.200
7723.89	-0.534	0.0100	0.711	0.0300	0.007	0.294
7722.12	-0.508	0.0100	0.619	0.0300	0.000	0.200
7720.29	-0.480	0.0255	0.611	0.0596	0.000	0.200
7702.54	-0.413	0.0236	0.509	0.0597	0.006	0.254
7693.76	-0.454	0.0100	0.582	0.0300	0.000	0.200
7691.94	-0.453	0.0100	0.580	0.0300	0.000	0.200
7690.17	-0.457	0.0100	0.598	0.0300	0.222	0.228
7688.39	-0.454	0.0100	0.530	0.0300	0.000	0.200

Table 6—Continued

Velocity km s ⁻¹	X mas	X _σ mas	Y mas	Y _σ mas	A km s ⁻¹ yr ⁻¹	A _σ km s ⁻¹ yr ⁻¹
7686.66	-0.469	0.0169	0.575	0.0472	0.000	0.200
7684.84	-0.445	0.0122	0.599	0.0336	0.000	0.200
7683.11	-0.437	0.0117	0.604	0.0339	0.000	0.200
7681.29	-0.444	0.0128	0.591	0.0351	0.000	0.200
7626.26	-0.368	0.0100	0.448	0.0300	0.000	0.200
7624.49	-0.362	0.0100	0.473	0.0300	0.000	0.200
7622.71	-0.354	0.0114	0.450	0.0322	0.000	0.200
7620.94	-0.364	0.0134	0.528	0.0343	0.000	0.200
7619.16	-0.360	0.0148	0.461	0.0378	0.000	0.200
7601.44	-0.376	0.0140	0.508	0.0406	0.000	0.200
7599.67	-0.344	0.0165	0.408	0.0480	0.000	0.200
7597.83	-0.379	0.0214	0.416	0.0500	0.000	0.200
7596.06	-0.400	0.0272	0.418	0.0636	0.000	0.200
7592.54	-0.380	0.0132	0.544	0.0361	0.000	0.200
7590.76	-0.332	0.0115	0.344	0.0306	0.000	0.200
7588.99	-0.347	0.0100	0.396	0.0300	0.000	0.200
7587.21	-0.351	0.0105	0.421	0.0300	0.000	0.200
7583.64	-0.356	0.0100	0.411	0.0300	-0.528	0.228
7581.89	-0.356	0.0100	0.444	0.0300	0.000	0.200
7578.34	-0.356	0.0104	0.412	0.0300	0.000	0.200
7576.56	-0.344	0.0106	0.396	0.0300	0.000	0.200
7574.81	-0.342	0.0153	0.410	0.0445	0.000	0.200
7572.99	-0.388	0.0252	0.452	0.0589	0.000	0.200
7555.24	-0.336	0.0237	0.364	0.0556	0.000	0.200
7549.94	-0.336	0.0103	0.323	0.0300	-0.175	0.211
7548.16	-0.334	0.0100	0.389	0.0300	0.000	0.200
7546.41	-0.325	0.0171	0.367	0.0497	0.000	0.200
7544.63	-0.363	0.0165	0.370	0.0478	0.000	0.200
7541.08	-0.334	0.0110	0.331	0.0319	0.000	0.200
7539.30	-0.342	0.0100	0.355	0.0300	0.100	0.213
7537.53	-0.306	0.0141	0.312	0.0409	0.000	0.200
7542.85	-0.306	0.0157	0.334	0.0455	0.000	0.200

Note. — Input data for the Bayesian fitting program for NGC 5765b. No error floor for the position data has been added. An error floor of 0.2 km s⁻¹ yr⁻¹ was added for the acceleration data of the high-velocity masers.

Table 7. Disk Fitting Results from NGC5765b

Parameter	Priors	Posterioris	Units
H_0	...	66.0 ± 5.0	$\text{km s}^{-1} \text{Mpc}^{-1}$
M	...	4.55 ± 0.31	$10^7 M_\odot$
V	8304 ± 30	8334.60 ± 1.13	km s^{-1}
X_0	...	-0.044 ± 0.0025	mas
Y_0	...	-0.100 ± 0.0025	mas
i_0	...	94.5 ± 0.25	deg
di/dr	...	-10.6 ± 1.13	deg mas^{-1}
p_0	...	146.7 ± 0.125	deg
dp/dr	...	-3.46 ± 0.43	deg mas^{-1}
V_{cor}	0 ± 250	2.0 ± 282	km s^{-1}

Note. — Fitting results for the global parameters describing the maser disk, which are Hubble constant (H_0); black hole mass (M); recession velocity of NGC 5765b, with optical definition (V); position of the dynamic center (X_0 , Y_0); inclination of the disk (i_0); warping of the disk on the inclination angle direction (di/dr); position angle of the disk (p_0); warping of the disk on the position angle direction (dp/dr); velocity correction due to any peculiar motion of NGC 5765b with respect to the Hubble flow (V_{cor}). For each parameter, we quote the mean value in its probability distribution function as the fitted result, and 68% confidence range as the error. All uncertainties listed here have been scaled by $\sqrt{\chi^2/N}$, i.e., $\sqrt{1.575}$.

Table 8. Table of H_0 uncertainty terms

Formal uncertainty		H_0 (km s ⁻¹ Mpc ⁻¹)	1 σ Uncertainty (km s ⁻¹ Mpc ⁻¹)	(%)
Base model		66.0	± 5.0	7.6
Systematic uncertainties	Value in Base Model	H_0 (km s ⁻¹ Mpc ⁻¹)	Difference from base model (km s ⁻¹ Mpc ⁻¹)	(%)
Different systemic feature				
acceleration error floor	...	68.0	2.0	3.00
Different hv-feature				
acceleration error floor	0.2 km s ⁻¹ yr ⁻¹	66.5	0.5	0.75
Different method for measurement				
of systemic accelerations	...	68.5	2.5	3.8
Unmodeled spiral structure	0.66	1.0
Systematic uncertainties				
added in quadrature			3.31	5.0
Uncertainty in the H_0 based				
on NGC 5765b maser distance			6.0	9.1

Note. — The final uncertainty is calculated by adding individual sources of uncertainty in quadrature.

Table 9. Comparison of input data between NGC 4258 and NGC 5765b

Name	Red-shifted	Systemic	Blue-shifted
Number of data points			
NGC 4258	151	187	32
NGC 5765b	71	71	70
Velocity Range (km s ⁻¹)			
NGC 4258	420	195 (110)	236
NGC 5765b	354	90 (70)	253

Note. — Comparison of the input data for the Bayesian fitting between NGC 4258 and NGC 5765b. For the velocity range of systemic masers, the number listed in the brackets are velocity ranges with valid accelerations measured.